

An interface-enriched generalized finite element method for the analysis and topology optimization of 2-D electromagnetic problems

Steven van Bergen ^{a,1}, Richard A. Norte ^{a,b,2}, Alejandro M. Aragón ^{a,3,*}

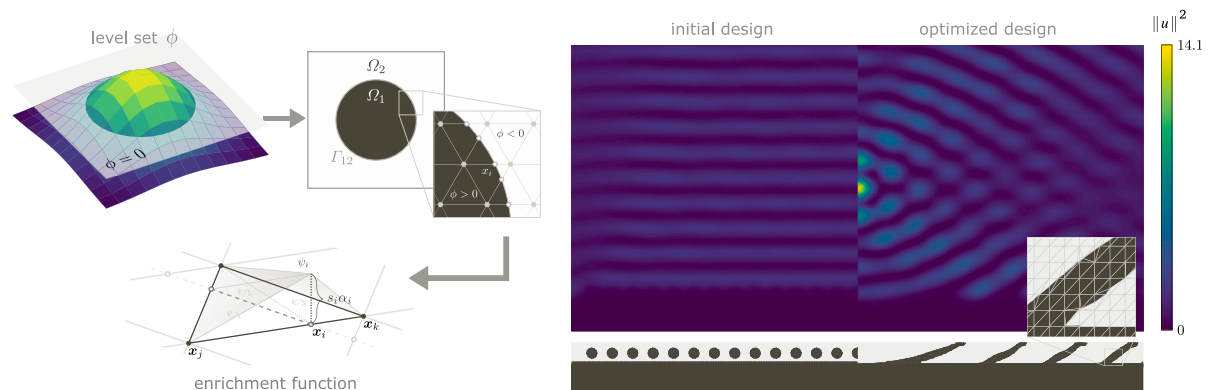
^a Faculty of Mechanical Engineering, Delft University of Technology, Mekelweg 2, 2628 CD Delft, The Netherlands

^b Kavli Institute of Nanoscience, Department of Quantum Nanoscience, Delft University of Technology, Lorentzweg 1, 2628CJ Delft, The Netherlands

GRAPHICAL ABSTRACT

METHODS: Enriched FEM is used to decouple geometry from the mesh

APPLICATION: An optimization of a reflector design



ARTICLE INFO

Keywords:

Enriched finite element analysis
Interface-enriched generalized finite element method (IGFEM)
Topology optimization
Electromagnetics
Level set method

ABSTRACT

The computational analysis of nanophotonic devices is usually carried out via the standard finite element method (FEM). However, FEM requires meshes that are fitted to the devices' boundaries, so making changes to the geometry (and thus the mesh) results in an inefficient process at best. Such an approach is therefore at odds when conducting design, which requires the analysis of multiple device geometries until reaching a satisfactory solution. Computational design tools such as topology optimization are often used, but the use of density-based representations of geometry inevitably leads to other issues—e.g., pixelized fuzzy boundaries

* Corresponding author.

E-mail address: a.m.aragon@tudelft.nl (A.M. Aragón).

URL: <https://www.tudelft.nl/staff/a.m.aragon> (A.M. Aragón).

¹ 0009-0007-7410-9657

² 0000-0003-1458-5735

³ 0000-0003-2275-6207

<https://doi.org/10.1016/j.cma.2024.116748>

Received 26 June 2023; Received in revised form 1 January 2024; Accepted 2 January 2024

Available online 6 February 2024

0045-7825/© 2024 The Author(s). Published by Elsevier B.V. This is an open access article under the CC BY license (<http://creativecommons.org/licenses/by/4.0/>).

with “gray material” (that does not correspond to dielectric nor vacuum) have an adverse effect on the devices’ interaction with electromagnetic waves.

In this paper we propose an interface-enriched generalized finite element method (IGFEM) for the analysis of two-dimensional electromagnetic scattering and eigenvalue problems. IGFEM enables the use of finite element meshes that are completely decoupled from the problem’s geometry. The analysis procedure is further coupled to a level set description of topology, resulting in a versatile enriched approach to topology optimization; this level set-based interface-enriched topology optimization procedure is devoid of the issues mentioned above regarding density-based methods, and yields crisp “black-and-white” designs that are devoid of jagged fuzzy edges. We first demonstrate that the analysis procedure achieves the same convergence rate as that of standard FEM using geometry-fitted meshes. We then compare the convergence properties of IGFEM with Nitsche’s method on a problem containing an embedded straight interface. Finally, we conduct topology optimization for designing both a 2-D metalen and a 2-D reflector, maximizing their ability to focus light onto a target point.

1. Introduction

Advancements in fabrication at the micro- and nano-scales have enabled the creation of nanophotonic devices that can be used to guide, confine, or even filter the flow of light in new ways that were not possible before [1]. Nanophotonic devices being investigated are, e.g., solar cells [2], highly-efficient lasers [3,4], and biosensors [5–7], which can be used to detect diseases [8,9]. However, the design of nanophotonic devices can be non-intuitive, especially for applications where multiple frequencies of light need to be controlled differently or for applications with nonlinear phenomena [10]. Consequently, computational tools such as parametric, shape, and topology optimization are increasingly being investigated.

Parametric optimization has been used for optimizing waveguides or resonant cavities while varying hole sizes and locations within the photonic crystal structure [11–14]. However, because of the limited number of design parameters, parametric optimization can only explore a limited range of designs, so performance is likely to be suboptimal. A less constrained optimization method, shape optimization, has also been applied to nanophotonic devices [4,15]. Although shape optimization gives more freedom in design compared to parametric optimization, it cannot change the topology, which may be required to reach a design with ultimate performance. By using topology optimization, we can freely change the material distribution allowing for more complex and non-intuitive designs.

Various topology optimization methods have been proposed in order to represent the material distribution inside of the computational design domain. In the commonly used density-based approaches, a density value is assigned to each element of the discretization. This density design variable varies continuously between zero (void) and one (solid material), thereby interpolating the properties of the design material. Because of intermediate density (gray) values, which do not correspond to either void nor solid material, a penalization scheme is usually applied to make gray values less attractive to the optimizer, thereby pushing the iterative algorithm to converge to designs that contain the minimum amount of gray material. Often, a filtering scheme, where element densities are defined as a weighted average of neighbouring elements, is applied to the design space to lessen numerical instabilities, i.e., checkerboarding patterns—alternating void and solid elements—and mesh dependency [16]. Although checkerboarding patterns do not arise in the design of photonic crystals, a filtering scheme can still be used to avoid mesh dependency [17]. However, using a filtering scheme introduces intermediate densities along boundaries of the design, thereby requiring a threshold projection to retrieve a black-and-white design. Occasionally, a more robust formulation including multiple thresholds at different levels is used to further enforce a minimum length scale—also known as a filtering-threshold scheme [16,18,19]. Density-based topology optimization has been applied to the design of photonic crystal band gaps [20], resonant cavities [21–25], waveguides [26–28], and photonic crystal modes with Dirac-like cones [29]. However, a disadvantage of this approach is the dependence on the (usually structured) finite element mesh used to discretize the computational design domain. Material interfaces that are not aligned with finite element edges can only be represented in a jagged manner. This has been shown to deteriorate the accuracy of simulations in phononic crystals (PnCs) (i.e. mechanical counterpart of photonic crystals), and consequently density-based methods require highly refined finite element discretizations to compensate for the loss of accuracy due to jagged boundaries [30]. In nanophotonics, surface roughness is known to cause scattering losses, reducing the efficiency and performance of nanophotonic devices [31]. When introducing small spatial variations in nanophotonics simulations—similar to the jagged boundary representation of a density-based topology optimization approach—a large impact on the efficiency of confinement and guiding of light has also been observed [32–34]. Consequently, it is important to choose an analysis technique that focuses on the quality of the geometrical description of material interfaces during the optimization process. One approach to that end is to use a level set function, whereby the zero contour delineates the material interfaces; this procedure results in smoother interfaces since finite elements can be cut in arbitrary directions by the zeroth-level contour. Although a level set might always have a clear boundary, it still needs to be projected to the finite element mesh for analysis. A possibility is to use the Ersatz material approach, which introduces a linear interpolation of material properties for elements along the boundary [35]. However, this results in intermediate values again that, as mentioned before, can deteriorate the accuracy of the reflections [36].

Mesh dependency issues can be resolved by means of enriched finite element methods, which add enrichment functions to the standard finite element approximation (h -FEM) to properly resolve the kinematics of material interfaces using an unfitted mesh. For

instance, an enriched FEM (E-FEM) has been proposed for solving problems with strong and weak discontinuities—discontinuities in the field itself or in its gradient, respectively—whereby enriched degrees of freedom (DOFs) are added at element level and are subsequently condensed out to save computational costs [37]. This elemental enrichment procedure has been recently explored for solving electrostatic problems [38] and extended for electrohydrodynamic modelling [39]. E-FEMs that create a nodal enriched field—as opposed to elemental enrichments—are more widely known. An example of such method is the eXtended/Generalized FEM (X/GFEM) [40,41], which has also been applied in electromagnetic analysis [42–46] and to optimize a magnetic actuator [47]. However, using X/GFEM introduces some challenges, e.g., ill-conditioned system matrices that require the use of Stable Generalized FEM (SGFEM) [48]. Other challenges include the need for special formulations when prescribing boundary conditions [49,50] and the careful choice of enrichment functions since some of them could degrade the accuracy of the method [49].

The Interface-enriched Generalized FEM (IGFEM) [51,52] is also a related enriched procedure that can be used to solve interface problems—i.e., problems with weak discontinuities. In IGFEM, enrichment functions are also added to enhance the standard finite element functional space. At variance with X/GFEM, where enrichments are associated with those of the original mesh, in IGFEM enrichments are associated with new nodes that are placed directly along discontinuities. This has many advantages with regards to X/GFEM: (i) Because enrichment functions vanish at mesh nodes, boundary conditions can be enforced strongly as in standard FEM [51], even on immersed boundaries [49]; (ii) Since enrichment functions are local to cut elements by construction, they are equally zero outside and thus there is no degraded accuracy in blending elements; (iii) IGFEM is stable regarding the condition number of system matrices, which grows at the same rate as that of standard FEM using fitted meshes [52]; and (iv) Smooth reactive traction profiles can be recovered in Dirichlet boundaries [49], something that cannot be achieved in X/GFEM even with the use of stabilization techniques [53]. IGFEM has already been used for the analysis [54,55] and parametric optimization [56] of electromagnetic problems using edge elements—elements where the degrees of freedom (DOFs) are assigned to their edges, showing promising results. Edge elements are commonly used in electromagnetic problems to prevent spurious solutions when the divergence conditions, which usually do not appear explicitly in the system equations, are not satisfied [57–59]. Nodal elements, i.e., elements where DOFs are assigned to nodes, do not always satisfy these divergence conditions. However, the 2-D formulation of Maxwell's equations, where only the out-of-plane electric and magnetic fields are solved, can be handled by the standard finite element method with nodal elements, since divergence conditions are satisfied automatically [57]. Compared to the order of local approximation error of nodal elements (which reduces with mesh size h as $\mathcal{O}(h^2)$), commonly used edge elements (Whitney 1 elements) have a local approximation error of the order $\mathcal{O}(h)$ [59]. Other types of edge elements, i.e., consistently linear edge elements, do yield the same local approximation error as nodal elements but they are computationally less efficient than nodal elements [59]. Moreover, the implementation of nodal elements is straightforward and they form the basis of most finite element softwares, thus allowing for the methods in this paper to be readily implemented in displacement-based finite element codes. However, the use of nodal elements in an interface-enriched procedure that decouples the finite element mesh from the problem's geometry is yet to be applied to electromagnetic problems.

In this paper we propose an enriched finite element method for the analysis and optimization—by means of topology optimization—of 2-D electromagnetic problems. At variance with the work of Zhang et al. [60], which uses edge elements, in this work we use nodal elements building on the work of van den Boom et al. [30]. First, a 2-D IGFEM-based electromagnetic analysis is proposed for harmonic scattering and eigenvalue problems. Band structure analysis is performed next on photonic crystal designs taken from Joannopoulos et al. [31] using h -FEM and IGFEM. A convergence analysis is performed on a simple Mie scattering problem for h -FEM and IGFEM, demonstrating that optimal convergence rates can be attained. Also, we compare the convergence properties of IGFEM with those of Nitsche's method for embedded interfaces by Zou et al. [61]. Finally, by building on the work of van den Boom et al. [62], we combine IGFEM with a level set description of topology to conduct computational design. We demonstrate that this level set-based interface-enriched topology optimization procedure, which has already been investigated for minimizing compliance [62], maximizing phononic band gaps [30], and for tailoring fracture resistance [63,64], can also be used for designing nanophotonic devices. We optimize a meta lens and a reflector for maximizing light intensity concentration, problems borrowed from Christiansen and Sigmund [65].

2. Formulation

Consider in Fig. 1 a domain $\Omega \subset \mathbb{R}^2$ composed of three subdomains Ω_1 , Ω_2 , and Ω_3 , such that $\bar{\Omega} = \bar{\Omega}_1 \cup \bar{\Omega}_2 \cup \bar{\Omega}_3$ and $\Omega_1 \cap \Omega_2 \cap \Omega_3 = \emptyset$. Subdomains Ω_1 and Ω_2 may correspond, for instance, to dielectric and vacuum regions (or vice versa). Ω_3 corresponds to an absorbing (vacuum) layer, discussed in detail in Section 2.3.1. The boundary to the i th subdomain is $\Gamma_i \equiv \partial\Omega_i = \bar{\Omega}_i \setminus \Omega_i$. The outward unit normal vector field to this boundary is denoted n_i . The interface between subdomains Ω_i and Ω_j is denoted as $\Gamma_{ij} = \bar{\Omega}_i \cap \bar{\Omega}_j$. We use the zeroth value of a level set function ϕ to describe Γ_{12} (see Fig. 1) and the outermost boundary (in the case of Fig. 1) by $\Gamma^o = \Gamma_3 \setminus \Gamma_{23}$ (or $\Gamma^o = \Gamma_2 \setminus \Gamma_{12}$ if $\Omega_3 = \emptyset$). We assume linear and isotropic media, and no sources inside of the domain, i.e., the electric current density (J) is zero.

Depending on the type of analysis, different boundary conditions are prescribed, including Dirichlet Γ^D and Neumann Γ^N boundary conditions (BCs). These boundary conditions will be further discussed in later sections. For 2-D problems, where we assume no variations in the medium and fields with respect to the out-of-plane z -direction, the electric and magnetic fields are decomposed into transverse magnetic (TM) and transverse electric (TE) polarizations. The TM case has a nonzero out-of-plane electric field (E_z) and in-plane magnetic field (H_x, H_y) and the TE case has a nonzero in-plane electric field (E_x, E_y) and out-of-plane magnetic field (H_z). As a result, the governing electromagnetic differential equations can be formulated with two scalar wave equations [57]:

$$\left[\frac{\partial}{\partial x} \left(\frac{1}{p} \frac{\partial}{\partial x} \right) + \frac{\partial}{\partial y} \left(\frac{1}{p} \frac{\partial}{\partial y} \right) + q \left(\frac{\omega}{c} \right)^2 \right] u + f = 0 \quad \text{in } \Omega, \quad (1)$$

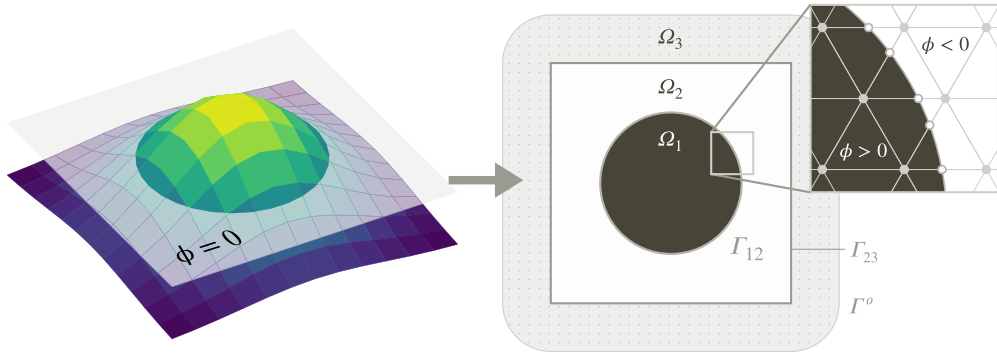


Fig. 1. Schematic of a domain Ω showing subdomains defined by a level set function ϕ . Subdomains Ω_1 and Ω_2 correspond to positive and negative values of ϕ , respectively, and are separated by the material interface Γ_{12} (i.e., the zeroth contour of ϕ). The subdomain Ω_3 with outer boundary Γ^o surrounds Ω_1 and Ω_2 . The inset shows the finite element discretization around the material interface that is not fitted to the interface. Standard mesh and enriched nodes are represented with \bullet and \circ symbols, respectively.

where for TM polarization, $u = E_z$, $p = \mu_r$ and $q = \epsilon_r$ and for TE polarization, $u = H_z$, $p = \epsilon_r$ and $q = \mu_r$. ω is the frequency (in radians), c is the speed of light, and f is the external source term that is dependent on the type of analysis, and will be further discussed in later sections. ϵ_r and μ_r are the relative permittivity and the relative permeability, respectively, which are taken relative to their counterparts in vacuum, denoted by ϵ_0 and μ_0 . In (1) u denotes the primal field, and because we have different subdomains, we denote u_i as the restriction of the primal field to the i th phase (either dielectric or vacuum), i.e., $u_i \equiv u|_{\Omega_i}$.

Given the prescribed primal field \bar{u} on Γ^D (i.e., the non-homogeneous Dirichlet boundary condition), find $v_i = u_i - \bar{u} \in \mathcal{V}_0$ (the unknown part of the solution) such that

$$B(v_i, w_i) = L(w_i) - B(\bar{u}, w_i) \quad \forall w_i \in \mathcal{V}_0, \tag{2}$$

where bilinear and linear forms in (1) are given respectively by

$$B(v_i, w_i) = \sum_{i=\{1,2\}} \int_{\Omega_i} \frac{1}{p_i} \frac{\partial w_i}{\partial x} \frac{\partial v_i}{\partial x} + \frac{1}{p_i} \frac{\partial w_i}{\partial y} \frac{\partial v_i}{\partial y} \, d\Omega - \omega^2 \sum_{i=\{1,2\}} \int_{\Omega_i} \frac{q_i}{c^2} w_i v_i \, d\Omega, \tag{3}$$

$$L(w_i) = \sum_{i=\{1,2\}} \int_{\Omega_i} w_i f_i \, d\Omega.$$

The trial function v_i and the test function w_i are both taken from the function space

$$\mathcal{V}_0(\Omega) = \left\{ v \in \mathcal{L}^2(\Omega), v_i \equiv v|_{\Omega_i} \in \mathcal{H}^1(\Omega_i), v|_{\Gamma^D} = 0 \right\}, \tag{4}$$

where $\mathcal{L}^2(\Omega)$ is the space of square-integrable functions and $\mathcal{H}^1(\Omega_i)$ is the first-order Sobolev space—the latter defined only on the individual phases. The fact that both v_i and w_i are taken from the same space—a Bubnov–Galerkin approach—will eventually yield symmetric system matrices [66, Chapter 2].

2.1. Interface-enriched generalized finite element analysis

To solve the finite-dimensional version of (3), we discretize the domain with a mesh of n_E non-overlapping triangular elements e_i such that $\Omega \approx \Omega^h = \text{int}(\cup_{i \in \mathcal{I}_h} \bar{e}_i)$, where $\text{int}(\cdot)$ denotes set interior. Following a Bubnov–Galerkin approach, we adopt the trial solution and the test function from the interface-enriched generalized finite element space given by [62]

$$\mathcal{V}_0^h = \left\{ v^h(x) \mid v^h(x) = \underbrace{\sum_{i \in \mathcal{I}_h} N_i(x) U_i}_{\text{standard FEM}} + \underbrace{\sum_{i \in \mathcal{I}_w} s_i \psi_i(x) \alpha_i}_{\text{enrichment}} \right\} \subset \mathcal{V}_0, \tag{5}$$

where \mathcal{I}_h and \mathcal{I}_w are index sets corresponding to standard FEM and enriched nodes, respectively. The first term consists of the standard finite element component, i.e., Lagrange shape functions $N_i(x)$ associated with their corresponding DOFs U_i for every node in \mathcal{I}_h . The second term enhances the standard FEM space by means of weakly-discontinuous (a discontinuity in the field gradient) enrichment functions $\psi_i(x)$, which capture the kinematics of phase interfaces Γ_{ij} . These functions are associated with their corresponding enriched DOFs α_i (see Fig. 2). The scaling factor s_i is used to produce a well-conditioned system as interfaces get arbitrarily close to standard nodes—thus producing small cuts. Scaling the enrichment functions actually yields condition numbers that grow at the same rate as those of standard nodal FEM, i.e., $\mathcal{O}(h^2)$ [52].

The finite element discretization Ω^h , when using IGFEM, is done without any knowledge of material discontinuities inside the domain. We use a level set function $\phi(x)$ to define material interfaces. Enriched nodes are then placed at the intersection locations

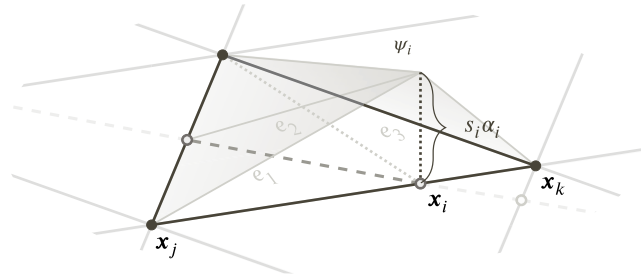


Fig. 2. Weak enrichment function ψ_i associated with the scaled enriched DOF $s_i \alpha_i$. x_i is the coordinate of the enriched node and x_j and x_k are the coordinates of the nodes that define the cut edge. The dashed line represents the discontinuity and the enriched nodes are represented by white nodes \circ .

of the zero contour of the level set function and element edges of the original mesh, thereby properly resolving the kinematics of the material interfaces. Part of the mesh, showing standard and enriched nodes, is shown in the inset of Fig. 1—notice that positive and negative level set values correspond to the different phases. The location of the i th enriched node x_i is found by

$$x_i = x_j - \frac{\phi(x_j)}{\phi(x_k) - \phi(x_j)}(x_k - x_j), \tag{6}$$

which is the linear interpolation of the level set function between nodes x_k and x_j at the ends of the intersected edge of an element of the mesh [62].

After adopting $u^h, v^h \in \mathcal{V}_0^h$, the finite-dimensional version of (3) is evaluated numerically. The computation of local arrays in uncut elements follows standard procedures. Cut elements, however, are usually subdivided in *integration elements* for Gauss quadrature [62]. This is done so that the numerical quadrature of local element arrays uses the least number of integration points (functions are smooth inside integration elements). For instance, the element shown in Fig. 2 is subdivided in three elements e_1 , e_2 , and e_3 . The local matrix k_e of the e th integration element is computed as

$$k_e = \int_{\mathfrak{L}} \mathbf{B}^T \mathbf{D}_e(p_e) \mathbf{B} \mathcal{J}_e \, d\xi, \tag{7}$$

where integration is conducted on the master element $\mathfrak{L} = \{ \xi = (\xi, \eta) \mid \xi \geq 0, \eta \geq 0, \xi + \eta \leq 1 \}$ and $\mathbf{B} = [\nabla_x N_1 \dots \nabla_x \psi_1 \dots]^4$ stacks the spatial derivatives of shape and enrichment functions. Noteworthy, we adopt an iso-parametric formulation, whereby the geometry and the primal fields are interpolated linearly. \mathcal{J}_e in (7) refers to the determinant of the Jacobian matrix associated with the integration element geometry mapping and the matrix \mathbf{D}_e is given by

$$\mathbf{D}_e(p_e) = \begin{bmatrix} 1/p_e & 0 \\ 0 & 1/p_e \end{bmatrix}. \tag{8}$$

The local matrix m_e of the e th integration element is computed as

$$m_e = \int_{\mathfrak{L}} \frac{q_e}{c^2} \mathbf{N}^T \mathbf{N} \mathcal{J}_e \, d\xi, \tag{9}$$

where $\mathbf{N} = [N_1 \dots \psi_1 \dots]^T$ stacks shape and enrichment functions. The global system matrices \mathbf{K} and \mathbf{M} can then be obtained by standard procedures, i.e.,

$$\mathbf{K} = \mathbb{A}_{e=1}^{n_E} k_e, \quad \mathbf{M} = \mathbb{A}_{e=1}^{n_E} m_e, \tag{10}$$

where \mathbb{A} denotes the standard finite element assembly operator. The final set of equations depends on the type of analysis and will be described in further sections. Further details on the formulation can be found in Aragón et al. [52], van den Boom et al. [62], Aragón and Duarte [66, Chapter 5], and references therein.

2.2. Band structure analysis

Commonly used in nanophotonics are photonic crystals (PtCs), which are materials with periodic structures that cause interference of light—also known as Bragg scattering—to create frequency bands in which light is attenuated (i.e., band gaps) [31]. In order to reveal band gaps, a band structure analysis is usually conducted where multiple eigenvalue analyses are conducted to

⁴ Note that, because of the geometry mapping, the derivatives with respect of the global coordinates are computed by applying the chain rule. Note also that the quadrature over the integration element involves two mappings (parent and integration elements). Since quadrature is conducted on the integration element, an inverse mapping is needed to compute the master coordinate of the parent uncut element, which is needed to evaluate the Lagrangian shape functions N_i .

find the frequencies of the harmonic modes for all propagation directions of light, defined by the wave vector κ . For this analysis no absorbing layers are used ($\Omega_3 = \emptyset$) and there are no external sources ($f = 0$). It is assumed that the boundaries of the domain are periodic—the repeating building block of the photonic crystal, also known as the periodic unit cell, is repeated infinitely. Therefore, Bloch–Floquet boundary conditions are prescribed on the outer boundary Γ^o as

$$u(\mathbf{x}_s) = e^{j\kappa \cdot \mathbf{a}_i} u(\mathbf{x}_m), \quad (11)$$

where j is the complex number and \mathbf{x}_m and \mathbf{x}_s are the coordinates of a master and a slave node, respectively. These nodes are on either side of two connected boundaries and are separated by exactly one lattice vector \mathbf{a} , which describes the spatial frequency and direction of the periodic boundary. While (11) refers to standard FEM nodes, the case where an enriched node is located along the periodic boundary, the enriched DOF α_i do not correspond directly to the electric or magnetic field at the location of the enriched node. Instead, the original DOFs in support of the enriched node must also be taken into account as shown in (5). Substituting (5) into (11) yields

$$\alpha_s = \frac{e^{j\kappa \cdot \mathbf{a}}}{s_s \psi_s(\mathbf{x}_s)} \left[\sum_{i \in \iota_m} N_i(\mathbf{x}_m) U_i + s_m \psi_m \mathbf{x}_m \alpha_m \right] - \frac{1}{s_s \psi_s(\mathbf{x}_s)} \sum_{i \in \iota_s} N_i(\mathbf{x}_s) U_i, \quad (12)$$

where ι_m and ι_s are the sets of master and slave, respectively [50]. The Bloch–Floquet BCs is enforced through a transformation matrix \mathbf{Q} , containing the complex components from (11) and (12). The system matrices \mathbf{K} and \mathbf{M} will be multiplied with \mathbf{Q} , reducing the total amount of DOFs as the slave node DOFs are removed from the system

$$\begin{aligned} \tilde{\mathbf{K}}(\kappa) &= \mathbf{Q}^H(\kappa) \mathbf{K} \mathbf{Q}(\kappa), \\ \tilde{\mathbf{M}}(\kappa) &= \mathbf{Q}^H(\kappa) \mathbf{M} \mathbf{Q}(\kappa). \end{aligned} \quad (13)$$

These matrices can then be used for performing eigenvalue analysis for a set of wave vectors κ_j , resulting in the system

$$\left(\tilde{\mathbf{K}}(\kappa_j) - \omega_j^2 \tilde{\mathbf{M}}(\kappa_j) \right) \mathbf{U}_j = \mathbf{0}, \quad (14)$$

where the eigenfrequencies ω_j and the corresponding eigenvectors \mathbf{U}_j will both be unknown.

2.3. Scattering analysis

This type of analysis is used to investigate the scattering by various dielectric objects of an incoming light source, where all fields are assumed to be harmonic. Within computational electromagnetics, both Dirichlet and Neumann BCs imply we have a perfect electric (or magnetic) surface—an ideal material with infinite conductivity. In this work, these boundary conditions are used to model symmetric or asymmetric conditions that can reduce computational resources. Homogeneous Dirichlet BCs prescribe asymmetry condition and homogeneous Neumann BCs symmetry, for both TM and TE polarization [67].

2.3.1. Absorbing boundary conditions

All problems in this work are modelled using finite domains, however for scattering problems the domain is assumed to be unbounded [68]. Therefore, a proper method is needed to prevent numerical reflections that emerge at the outer boundary Γ^o . In this work we chose to attenuate outgoing waves by using Locally-Conformal Perfectly Matched Layers (LC-PMLs) [69]. A LC-PML adds an artificial absorbing (vacuum) layer Ω_3 (see Fig. 3), attenuating any outgoing waves irrespective of the incident angle and polarization. The disadvantage of the LC-PML compared to a prescribed absorbing boundary condition (ABC) on Γ^o is that the former increases the number of DOFs because of the added area around the original simulation domain. The LC-PML, however, has improved accuracy [68], can be implemented closer to the scatterer than an ABC [69], and works for any shaped region as long as it is convex; this makes LC-PMLs applicable to complex problems using only a single formulation, unlike ABCs whose formulation depends on the geometry of the domain [69]. The LC-PML is based on a locally defined complex coordinate transformation, whereby each coordinate \mathbf{x} within the PML region (Ω_3) is mapped to $\tilde{\mathbf{x}}$, i.e.,

$$\tilde{\mathbf{x}} = \mathbf{x} + \frac{1}{j\kappa} g(\zeta) \hat{\mathbf{n}}(\zeta), \quad (15)$$

where $\kappa = \omega \sqrt{\epsilon \mu}$ is the wave number, $\hat{\mathbf{n}}(\zeta)$ is a unit vector defined as $\hat{\mathbf{n}} = (\mathbf{x} - \mathbf{x}_0) / \zeta$, with $\zeta = \|\mathbf{x} - \mathbf{x}_0\|$ and $\mathbf{x}_0 = \operatorname{argmin}_{\mathbf{x}_i \in (\Gamma_3 \setminus \Gamma^o)} \|\mathbf{x} - \mathbf{x}_i\|$ being the coordinate of the closest point on the inner PML boundary. Because of the convexity of the PML boundary, \mathbf{x}_0 is uniquely defined. In (15) the function $g(\zeta)$ is a monotonically increasing function of ζ , being zero at the inner PML boundary to prevent numerical reflections:

$$g(\zeta) = \frac{\nu \zeta^w}{w \|\mathbf{x}_1 - \mathbf{x}_0\|^{w-1}}, \quad (16)$$

where ν is a positive parameter and w is a positive integer that determines the decay rate inside of the PML region, \mathbf{x}_1 is the coordinate of a point located at the intersection between the outer PML boundary (Γ^o) and a line passing through \mathbf{x}_0 and \mathbf{x} .

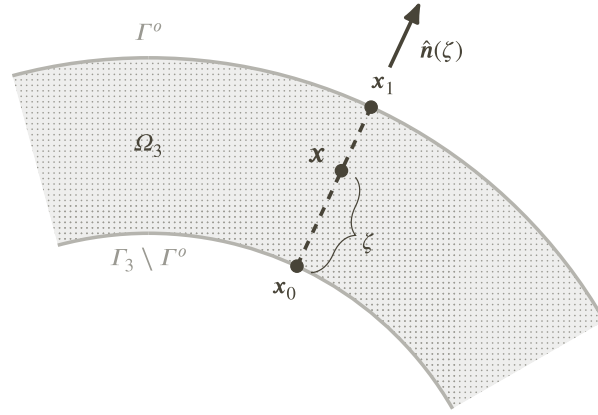


Fig. 3. Schematic of the LC-PML (shaded region). x is an arbitrary coordinate inside this region, and points x_0 and x_1 lie on the inner and outer boundary of the PML region, respectively. $\hat{n}(\zeta)$ is the normal vector to the boundary Γ^o from x_0 to x and ζ is the distance between x_0 to x .

2.3.2. Incoming plane waves

Electromagnetic waves entering from outside the domain (e.g., plane waves) are often implemented using a boundary condition. However, because of the PMLs enclosing our domain, we cannot implement it this way since the wave would have to travel through the absorbing layer. Instead, we use a scattered field formulation, where the total electric field u is decomposed into the *incoming field* \tilde{u} (the incident field produced without the scatterer) and the *scattered field* u^s (the resulting field produced by imposing the equivalent current on the surface inside the domain) [69–71]. The current should, however, only be imposed on the dielectric domain (i.e., Ω_d). Using the scattered field formulation the source term to the right hand side of (1) is

$$f = \left[\frac{\partial}{\partial x} \left(\frac{1}{p} \frac{\partial}{\partial x} \right) + \frac{\partial}{\partial y} \left(\frac{1}{p} \frac{\partial}{\partial y} \right) + q \left(\frac{\omega}{c} \right)^2 \right] \tilde{u}, \quad \text{for } x \in \Omega_d \quad (17)$$

where \tilde{u} is the incident field; this field can be arbitrary, but it is usually chosen to be a plane wave because the source is far enough away from the scatterer. In the case of a plane wave, the incident field can be described as

$$\tilde{u}(x) = u_0 e^{-j\kappa_0(x \cos \varphi + y \sin \varphi)}, \quad (18)$$

where $\kappa_0 = \omega \sqrt{\epsilon_0 \mu_0}$, u_0 is the amplitude of the incoming plane wave and φ is the incident angle of the plane wave, with $\varphi = 0$ being an incident angle along the positive x -axis.

When using an enriched formulation, the enriched DOFs α_i do not correspond directly to the electric nor magnetic field at the location of the enriched node. Instead, the original DOFs in support of the enriched node must also be taken into account (refer back to (5)). The enriched incoming field terms $\tilde{\alpha}_i$ are calculated as the difference between the interpolated incoming field from the original mesh nodes and the actual value at the enriched node location, i.e.,

$$\tilde{\alpha}_i = \frac{1}{s_i \psi_i(x_i)} \left(\tilde{u}(x_i) - \sum_{j \in I_h} N_j(x_i) \tilde{U}_j \right), \quad (19)$$

where x_i is the coordinate of the enriched node, $\psi_i(x)$ its associated enrichment function, $N_j(x)$ and \tilde{U}_j are the shape functions and corresponding incident field values of the original mesh nodes with index set I_h . To regain the total field, the computed scattered and incoming fields are added together. The addition of the scattered and incoming fields inside of the PML region will not create a physical result, so after the addition, the DOFs of the total field inside the PML region are set to zero. Since (17) is the same form as the governing equations, the system matrices \mathbf{K} and \mathbf{M} can be used together with a transformation matrix \mathbf{T} —a matrix with all DOFs inside the dielectric region set to one [69]. When using IGFEM, these DOFs also include the DOFs of the original mesh nodes connected to the enriched nodes. This will result in the system

$$(\mathbf{K} - \omega^2 \mathbf{M}) U^s = -\mathbf{T} (\mathbf{K} - \omega^2 \mathbf{M}) \tilde{U}, \quad (20)$$

where U^s contains the scattered field values.

2.3.3. Far-field calculation

A common use for electromagnetic scattering problems is to investigate the Radar Cross Section (RCS), which describes the far field reflections of an incident plane wave by a scatterer. In 2D, the RCS is defined as [69,70]

$$\sigma_{2D} = \lim_{R \rightarrow \infty} 2\pi R \frac{|u^f|^2}{|\tilde{u}|^2}, \quad (21)$$

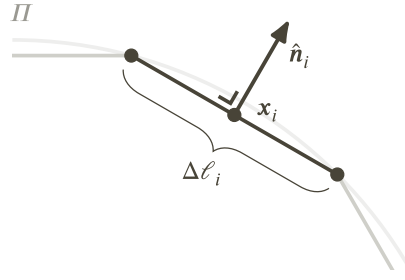


Fig. 4. A schematic showing the i th segment with its edge along Π and the associated variables.

where u^f is the scattered far-field and R is the observation radius from the scatterer; the latter should satisfy $R \gg 2D/\lambda_0$, where D is the largest dimension of the scatterer and λ_0 is the wavelength in vacuum. The far-field u^f can be calculated as a post-processing step with Huygens' surface equivalence principle, integrating the surface electric and magnetic current densities over a circular interface Π enclosing the scatterer. The integration over Π is done by subdividing the interface into smaller segments, then summing up the contribution of each segment, as shown in Fig. 4. The far-field can be calculated [69] as

$$u^f = \sqrt{\frac{\kappa_0}{8\pi R}} e^{j\pi/4} e^{-jk_0 R} \sum_{i \in \iota_f} (\hat{\mathbf{n}}_i \cdot \mathbf{e}_x \cos \theta + \hat{\mathbf{n}}_i \cdot \mathbf{e}_y \sin \theta) u_i e^{jk_0(x_i \cos \theta + y_i \sin \theta)} \Delta \ell_i + \frac{1}{j\omega} \sqrt{\frac{\kappa_0}{8\epsilon_0 \mu_0 \pi R}} e^{-j3\pi/4} e^{-jk_0 R} \sum_{i \in \iota_f} \left(\hat{\mathbf{n}}_i \cdot \mathbf{e}_x \frac{\partial}{\partial x} + \hat{\mathbf{n}}_i \cdot \mathbf{e}_y \frac{\partial}{\partial y} \right) u_i e^{jk_0(x_i \cos \theta + y_i \sin \theta)} \Delta \ell_i, \quad (22)$$

where ι_f is the set of segments along Π , $\hat{\mathbf{n}}_i$ is the outward facing unit normal vector of the i th segment with length $\Delta \ell_i$, \mathbf{e}_x and \mathbf{e}_y the Cartesian coordinate basis vectors, θ is the observation angle, and u_i , x_i and y_i the total field strength and x - and y -coordinates evaluated at the midpoint of the i th segment, respectively. Note that Π is not a meshed interface and thus the discretization can still happen without any prior knowledge about the geometry inside the domain.

2.4. Topology optimization

The topology optimization methodology in this work combines a level set function to describe the topology with the IGFEM-based analysis procedure described in the previous sections. As discussed earlier, enriched nodes are added along vacuum-dielectric interfaces to improve the accuracy of the analysis (see Eq. (6)). These interfaces are described by the zeroth value of the level set function, which is also decoupled from the analysis mesh to have more control on the design space. Therefore, the level set function uses compactly supported Radial Basis Functions (RBF) [62]. The i th RBF centred at coordinate \mathbf{x}_i is given by

$$\Theta_i(\zeta_i) = (1 - \zeta_i)^4 (4\zeta_i + 1), \quad (23)$$

where $\zeta_i(\mathbf{x}, \mathbf{x}_i) = \sqrt{\|\mathbf{x} - \mathbf{x}_i\|/\zeta_s}$ and ζ_s is the radius of support. Using RBFs the level set function is interpolated as

$$\phi(\mathbf{x}) = \sum_{i \in \iota_d} \Theta_i(\mathbf{x}) d_i = \Theta(\mathbf{x})^\top \mathbf{d}, \quad (24)$$

where ι_d is the index set of all design variables d_i . Evaluating this function over all original mesh nodes results in

$$\boldsymbol{\phi} = \boldsymbol{\theta}^\top \mathbf{d} \quad (25)$$

where $\boldsymbol{\theta}$ is a matrix containing all RBF values. RBFs give the design variables on every node a range of influence over other design variables nearby, giving the possibility to yield smooth designs—this works similarly to a density filter in standard density-based topology optimization. Note that during the optimization process, no stabilization or mass conservation methods are used for the level set. For more details, the reader is referred to van den Boom et al. [62].

2.4.1. Objective function and analytical sensitivity analysis

As an example, we implement a figure of merit to focus an incoming plane wave onto one or multiple chosen points. This problem was investigated by Christiansen and Sigmund [65], who used a density-based topology optimization approach. Mathematically, the objective function can be formulated as the weighted sum of light intensity $\|u\|^2$ at chosen nodes in the mesh. The optimization problem then becomes

$$\begin{aligned} \min_{\mathbf{d}} \quad & \Psi = -\mathbf{U}^H \mathbf{P} \mathbf{U} \\ \text{subject to} \quad & (\mathbf{K}(\mathbf{d}) - \omega^2 \mathbf{M}(\mathbf{d})) \mathbf{U}^s = -\mathbf{T} (\mathbf{K}(\mathbf{d}) - \omega^2 \mathbf{M}(\mathbf{d})) \tilde{\mathbf{U}}, \\ & \mathbf{d}_{\min} \leq \mathbf{d} \leq \mathbf{d}_{\max} \end{aligned} \quad (26)$$

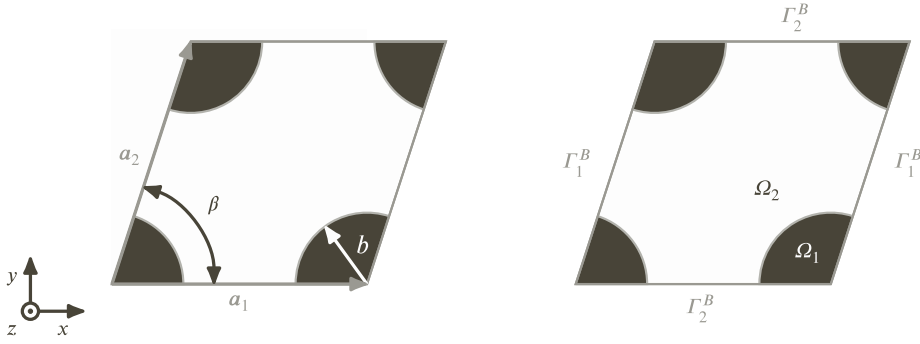


Fig. 5. Illustration of a photonic crystal unit cell (left) for an arbitrary lattice with angle β and a circular inclusion with radius b . Computational domain and boundary conditions (right) used for the simulation.

with \mathbf{P} being a diagonal matrix that selects and weights the points at which to maximize the light intensity, the superscript H denotes the conjugate transpose, and d_{\min} and d_{\max} are the lower and upper bounds of the design variables d_i , which are used to prevent the level set function from becoming too steep. At variance with compliance optimization problems, no volume constraint is used in this work since completely solid or void designs are not optimal. The level set function is updated using the Method of Moving Asymptotes (MMA) [72], which also requires the sensitivities of the objective with respect to the design variables. These are calculated analytically as

$$\frac{\partial \Psi}{\partial d_i} = \frac{\partial \Psi}{\partial \mathbf{U}_k} \frac{\partial \mathbf{U}_k}{\partial \phi_j} \frac{\partial \phi_j}{\partial d_i}. \quad (27)$$

The first term on the right-hand side of (27) is the derivative of the objective function with respect to the electric field values

$$\frac{\partial \Psi}{\partial \mathbf{U}_k} = -2\mathbf{U}_m^* P_{mk}, \quad (28)$$

where the superscript $*$ denotes complex conjugate. The second term is the derivative of the scattered electric field with respect to the j th level set value, which is calculated by solving the linear equation

$$(\mathbf{K} - \omega^2 \mathbf{M}) \frac{\partial \mathbf{U}_k^s}{\partial \phi_j} = \left(\frac{\partial \mathbf{K}}{\partial \phi_j} - \omega^2 \frac{\partial \mathbf{M}}{\partial \phi_j} \right) \mathbf{U}_k^s - \mathbf{T} \left[\left(\frac{\partial \mathbf{K}}{\partial \phi_j} - \omega^2 \frac{\partial \mathbf{M}}{\partial \phi_j} \right) \tilde{\mathbf{U}}_k + (\mathbf{K} - \omega^2 \mathbf{M}) \frac{\partial \tilde{\mathbf{U}}_k}{\partial \phi_j} \right], \quad (29)$$

after which the derivative of the incoming field can be added to get the total field derivative with respect to the j th level set value. Because (29) has the same left-hand side as (20), factorization of the system matrix, for example via LU decomposition, can be reused for efficiency. Finally, the third term is the derivative of the nodal level set values with respect to the design variables, which is computed as

$$\frac{\partial \phi}{\partial d} = \theta^\top, \quad (30)$$

where θ^\top is the matrix defined in (24) and (25). For more details see Appendix, which also contains a verification using a finite difference scheme.

3. Results

In this section three example problems are shown. First, band structure analysis is performed to find the dispersion relations of photonic crystal designs. Then, a Mie scattering problem, for which we have an exact solution, is solved on increasingly finer meshes for both the standard FEM and IGFEM, to obtain the convergence rates of the analysis procedure. Then, we compare our convergence rates to those of Nitsche's method on a problem containing an embedded straight interface. Finally, the topology optimization methodology is showcased in the design of both a 2-D metalens and a reflector. Note that throughout this section no units are given, so the results can be understood under any consistent unit system.

3.1. Band structure analysis

We consider a photonic crystal with a periodic unit cell containing a circular inclusion [31]. The unit cell is shown in Fig. 5, where b is the radius of the circular inclusion, β is the angle between the lattice vectors \mathbf{a}_1 and \mathbf{a}_2 , Ω_1 and Ω_2 are domains with relative permittivity ϵ_{r1} and ϵ_{r2} , respectively, and Γ_1^B and Γ_2^B are the regions of the boundary along the outer boundary Γ^o where Bloch–Floquet periodic BCs are prescribed. In all examples $\|\mathbf{a}_1\| = \|\mathbf{a}_2\| = a$, where a is also known as the lattice constant. As discussed earlier, in order to compute the complete band structure of a photonic crystal, an eigenvalue analysis must be done for

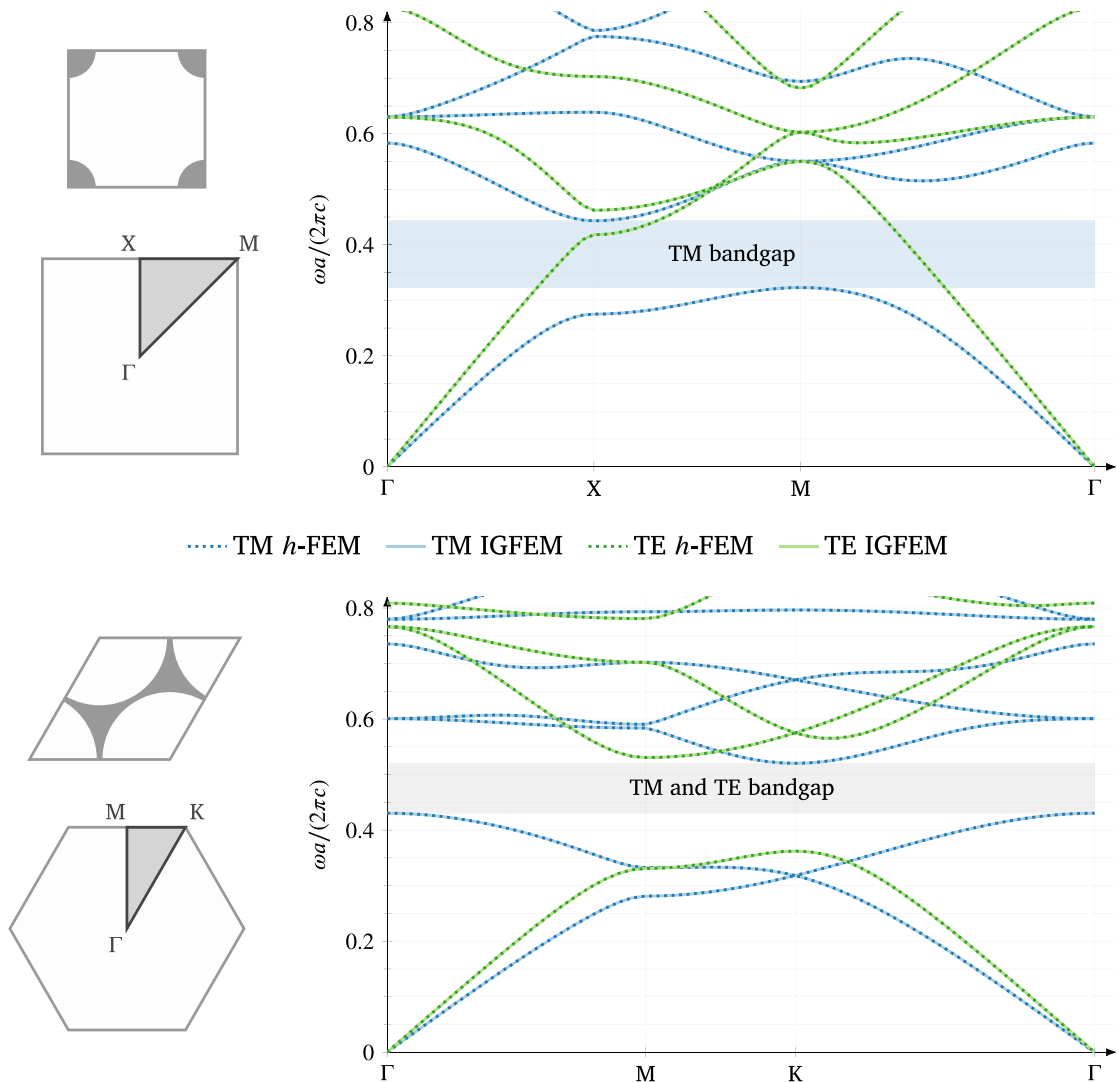


Fig. 6. Square (top row) and hexagonal (bottom row) periodic unit cells with their corresponding (irreducible) Brillouin zones (left) and obtained TM and TE band structures using *h*-FEM and IGFEM (right).

all wave vectors k . However, because of the translational and rotational symmetry of the photonic crystal lattice, the wave vectors that need to be considered can be reduced significantly. This collection of wave vectors is called the irreducible Brillouin zone.

Fig. 6 shows the band structure analysis of a square unit cell (top row) with $b = 0.2a$, $\beta = 90^\circ$, $\epsilon_{r1} = 8.9$ and $\epsilon_{r2} = 1$, and a hexagonal unit cell (bottom row) with $b = 0.48a$, $\beta = 60^\circ$, $\epsilon_{r1} = 1$ and $\epsilon_{r2} = 13$. For each, the unit cell with the corresponding (irreducible) Brillouin zone is shown (left), together with the computed band structure for both TM and TE modes (right); the analysis was done for both *h*-FEM and IGFEM with a mesh size of $h = 3a/100$. It can be seen that there is no noticeable difference between the band structure results obtained using *h*-FEM and IGFEM. The results of the obtained band structures also correspond with those found by Joannopoulos et al. [31].

3.2. Convergence study

In this section we conduct convergence analysis to obtain the rates of convergence of IGFEM on 2-D electromagnetic problems. To that end we solve a Mie scattering problem, which describes the scattering of an electromagnetic plane wave with a cylinder, and for which an analytical solution is available.

Consider a dielectric cylinder Ω_1 (shown in Fig. 7) with radius r and relative permittivity $\epsilon_{r1} = 2$ for an incident plane wave with wavelength $\lambda = r$ and angle of incidence $\varphi = \pi/2$ (towards the positive y direction). The dielectric is surrounded by a vacuum layer Ω_2 ($\epsilon_{r2} = 1$) with thickness $t_v = 0.4r$ and a PML region Ω_3 with thickness $t_{PML} = 0.7r$ is placed around the edges of the domain

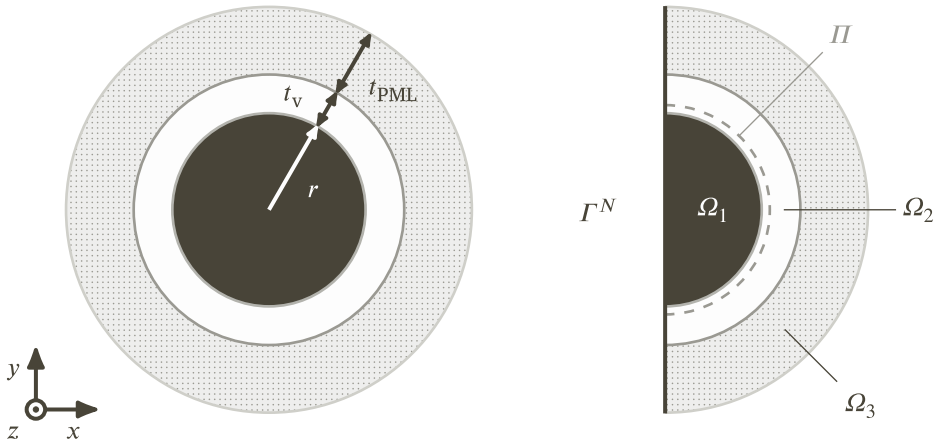


Fig. 7. Schematic of the Mie scattering problem used for the convergence analysis (left) and computational domain used for the simulation accounting for symmetry (right).

to absorb outgoing waves reflected by the scatterer. All domains have a relative permeability of $\mu_r = 1$. Γ^N is the boundary with prescribed homogeneous Neumann BC for symmetry, and Π is the Huygens surface used for the computation of the RCS.

Using wave transformation, a plane wave with unity magnitude and angle of incidence φ can be expressed in terms of cylindrical waves

$$e^{-j\kappa_0(x \cos \varphi + y \sin \varphi)} = \sum_{n=-\infty}^{\infty} j^{-n} \mathcal{J}_n(\kappa_0 \rho) e^{jn(\theta - \varphi)}, \tag{31}$$

where \mathcal{J}_n is the n th order Bessel function of the first kind and ρ and θ are the radial coordinate and the azimuth, respectively. Using this assumption, the analytical scattered field u^a of a plane wave by a dielectric cylinder can be calculated with [70,73]

$$u^a = \begin{cases} \sum_{n=-\infty}^{\infty} \alpha_n \mathcal{H}_n^{(2)}(\kappa_0 \rho) e^{jn(\theta - \varphi)} & \text{for } \rho \geq r \\ \sum_{n=-\infty}^{\infty} \beta_n \mathcal{J}_n(\kappa \rho) e^{jn(\theta - \varphi)} - j^{-n} \mathcal{J}_n(\kappa_0 \rho) e^{jn(\theta - \varphi)} & \text{for } \rho < r \end{cases} \tag{32}$$

where the terms α_n and β_n are given by

$$\alpha_n = -j^{-n} \frac{\sqrt{p} \mathcal{J}'_n(\kappa_0 r) \mathcal{J}_n(\kappa r) - \sqrt{q} \mathcal{J}_n(\kappa_0 r) \mathcal{J}'_n(\kappa r)}{\sqrt{p} \mathcal{H}_n^{(2)'}(\kappa_0 r) \mathcal{J}_n(\kappa r) - \sqrt{q} \mathcal{H}_n^{(2)}(\kappa_0 r) \mathcal{J}'_n(\kappa r)} \tag{33}$$

$$\beta_n = \frac{j^{-(n+1)}}{\pi \kappa_0 r} \frac{2\sqrt{p}}{\sqrt{p} \mathcal{H}_n^{(2)'}(\kappa_0 r) \mathcal{J}_n(\kappa r) - \sqrt{q} \mathcal{H}_n^{(2)}(\kappa_0 r) \mathcal{J}'_n(\kappa r)}, \tag{34}$$

where, for a TM polarized plane wave $u^s = E_z^s$, $p = \mu_r$ and $q = \epsilon_r$, while for a TE polarized plane wave $u^s = H_z^s$, $p = \epsilon_r$ and $q = \mu_r$. \mathcal{J}'_n is the derivative of the n th-order Bessel function of the first kind, and $\mathcal{H}_n^{(2)}$ and $\mathcal{H}_n^{(2)'}$ are the n th-order Hankel function of the second kind and its derivative, respectively. Note that these equations are an approximation and the accuracy of the scattered field increases with the number of terms in (32) [70]. In this work we choose $n \in [-100 \dots 100]$.

We consider the Mie scattering problem for a TM and TE polarized plane wave. Both problems are solved using h -FEM together with a mesh that is conforming to the vacuum-dielectric interface (Γ_{12}). The same problem is solved with an unfitted mesh using IGFEM to resolve the field in the elements cut by the dielectric inclusion. Fig. 8 shows the scattered field for TM (top row) and TE (bottom row) polarizations, obtained via h -FEM (left) and IGFEM (right) with a mesh size $h = \lambda/10$. Using the exact solution (32) we study the relative element-wise error with respect to the analytical solution, which is computed as

$$\|\epsilon\|_{\mathcal{L}^2(e)} = \frac{\|u - u^h\|_{\mathcal{L}^2(e)}}{\|u\|_{\mathcal{L}^2(e)}} = \sqrt{\frac{\int_e (u - u^h)^H (u - u^h) \, de}{\int_e \|u\|^2 \, de}}. \tag{35}$$

Fig. 9 shows the element-wise error in the scattered field for TM (top row) and TE (bottom row) polarizations, respectively. The error in the PML region is not taken into account since the numerical solution in that region does not agree with the analytical solution.

We now conduct a convergence analysis for $h/\lambda = \{1/10, 1/25, 1/50, 1/100\}$ using both h -FEM and IGFEM, where the \mathcal{L}^2 -norm of the error is obtained by aggregating the element-wise error, i.e.,

$$\|\epsilon\|_{\mathcal{L}^2(\Omega)} = \frac{\|u - u^h\|_{\mathcal{L}^2(\Omega)}}{\|u\|_{\mathcal{L}^2(\Omega)}} = \sqrt{\frac{\sum_{e \in \Omega^h} \int_e (u - u^h)^H (u - u^h) \, de}{\sum_{e \in \Omega^h} \int_e \|u\|^2 \, de}}. \tag{36}$$

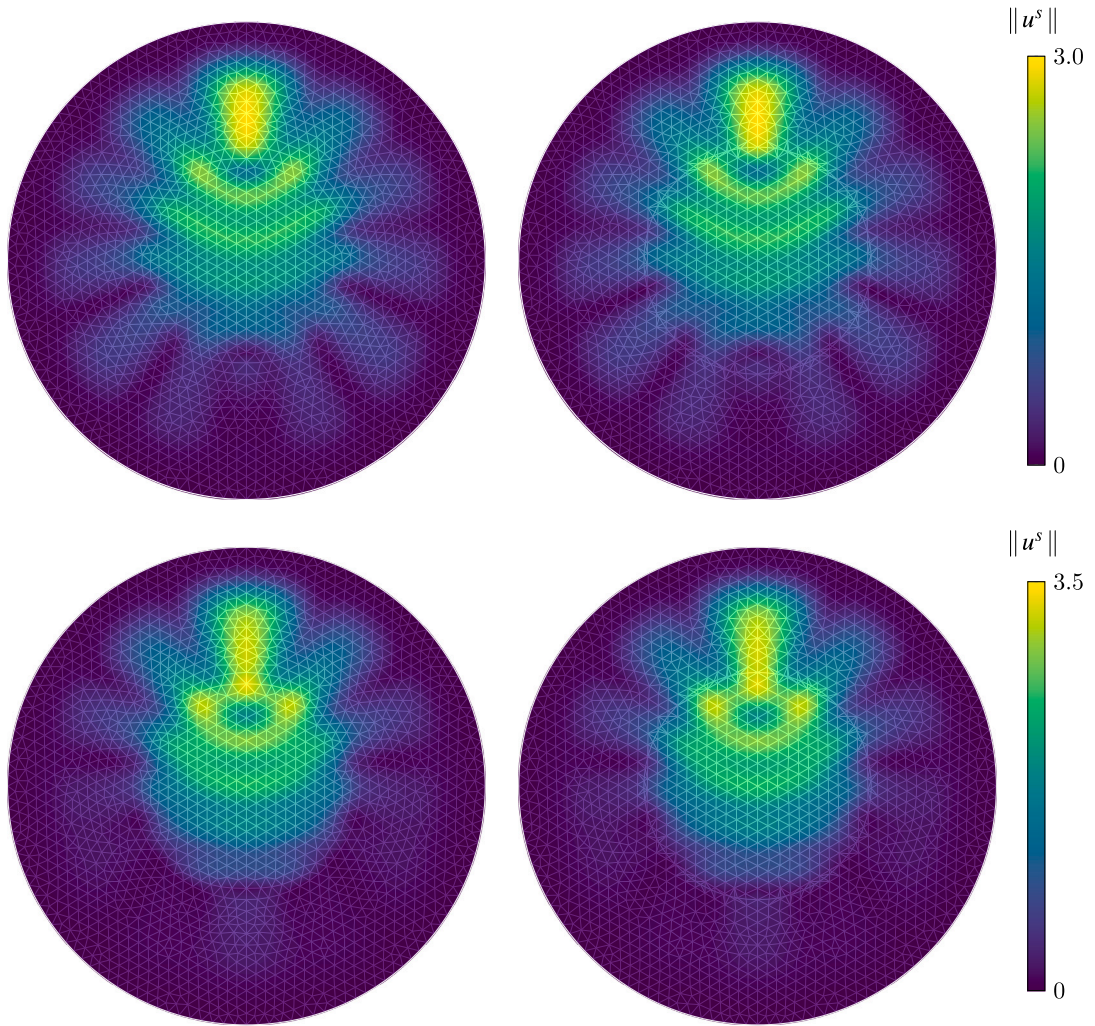


Fig. 8. The norm of the scattered field for TM (top row) and TE (bottom row) polarizations, obtained via h -FEM (left) and IGFEM (right).

This global error measure is plotted against the total number of degrees of freedom for both the TM and TE polarization cases in Fig. 10. In all cases, the convergence rate is -1 , which is the optimal rate for the L^2 -norm as a function of the number of DOFs. This means that the optimal convergence of h -FEM is recovered using IGFEM for electromagnetic problems. Note that, in addition to the optimal convergence rate, the accuracy of IGFEM is very similar to that of h -FEM.

Finally, the RCS is calculated for $h/\lambda = \{1/10, 1/25, 1/50, 1/100\}$ using the Mie scattering results obtained with h -FEM and IGFEM. For all examples $R = 100$ m and the interface Γ is subdivided into 100 segments and has a radius of $1.02r$. The analytical solution (32) is used to verify the RCS results. Fig. 11 shows the RCS for TM (top row) and TE (bottom row) polarizations, obtained with both h -FEM (left) and IGFEM (right). It can be seen that as the mesh size decreases, the computed RCS gets closer to the analytically calculated RCS.

3.3. Comparison with Nitsche's method

In this section we compare our approach with that of Zou et al. [61], who used Nitsche's method to enforce interfaces weakly in Helmholtz problems. For the comparison we will replicate their convergence study, but here we use IGFEM instead to resolve the interface.

Consider a rectangular domain (shown in Fig. 12) with $3W = 2L$, which is divided evenly into two subdomains Ω_1 and Ω_2 . The subdomains have relative permeabilities $\mu_{r1} = 1$ and $\mu_{r2} = 0.2$, respectively, and relative permittivities $\epsilon_{r1} = \epsilon_{r2} = c^2$. A homogeneous Dirichlet BC (i.e., $\bar{u} = 0$) is prescribed on the left edge Γ_1^D , and a non-homogeneous Dirichlet BC $\bar{u} = 1$ is prescribed on the right edge Γ_2^D . Γ^N is the boundary with prescribed homogeneous Neumann BC for symmetry. In order to make our problem the same as in Zou et al. [61], only the TM polarization is considered. Since the problem is essentially one-dimensional, the exact solution can be derived and used for a convergence analysis.

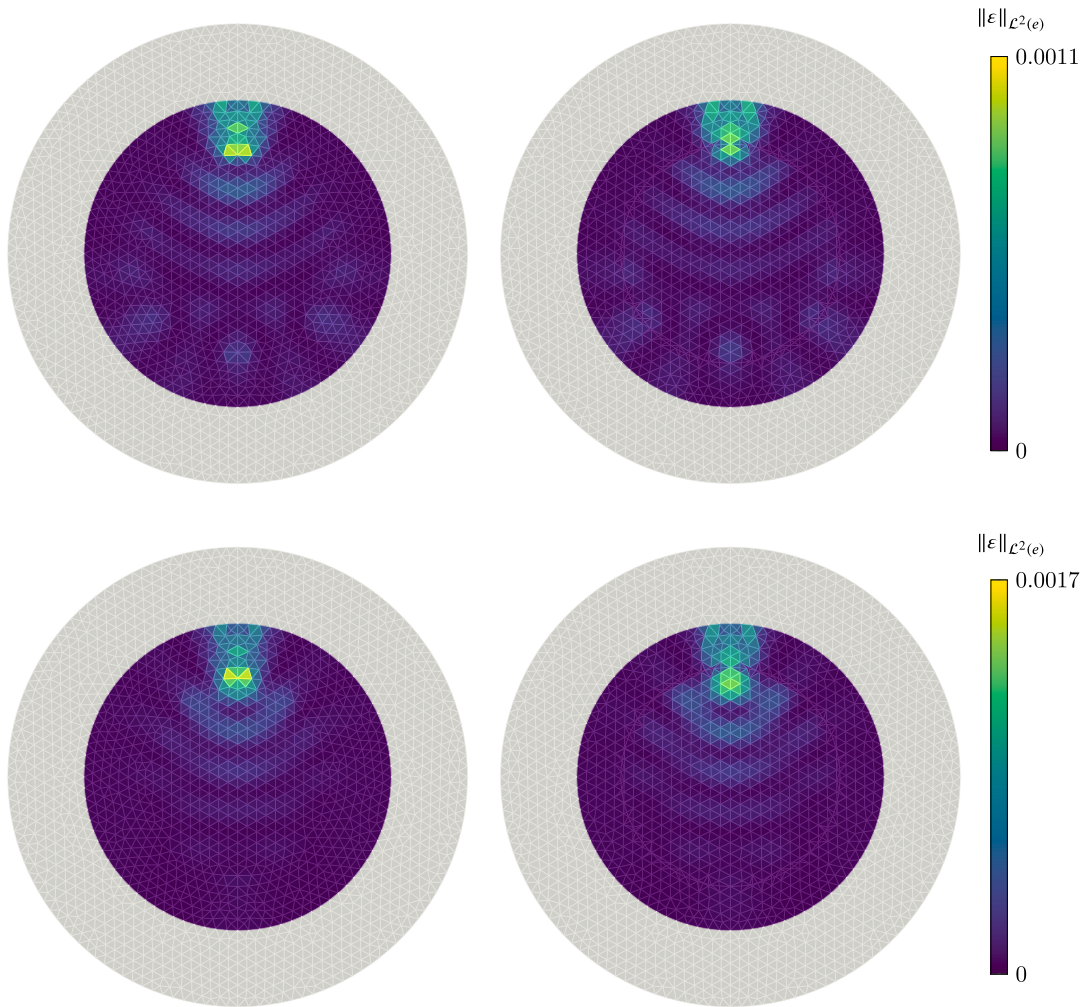


Fig. 9. L^2 -norm of the element-wise error for TM (top row) and TE (bottom row) polarizations obtained using h -FEM (left) and IGFEM (right). The PML region is coloured grey since the computed solution in that region does not agree with the analytical solution.

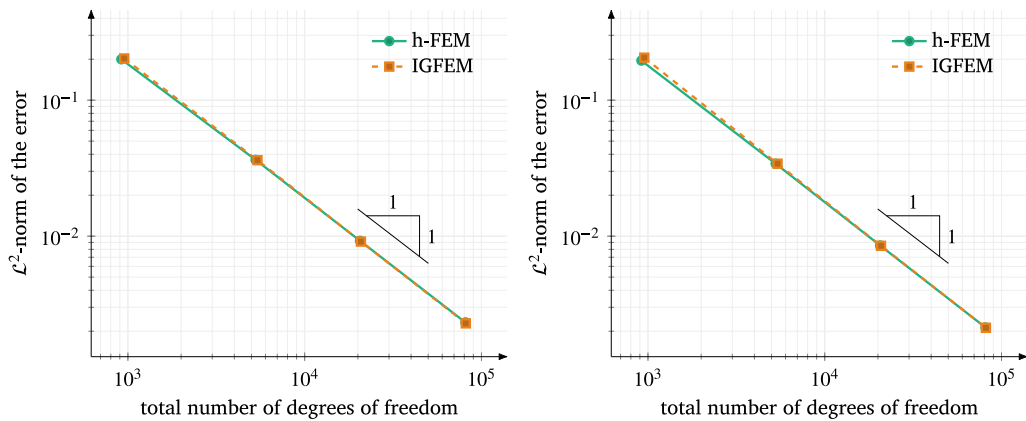


Fig. 10. L^2 -norm of the global error as a function of the total number of degrees of freedom for TM (left) and TE (right) polarization cases.

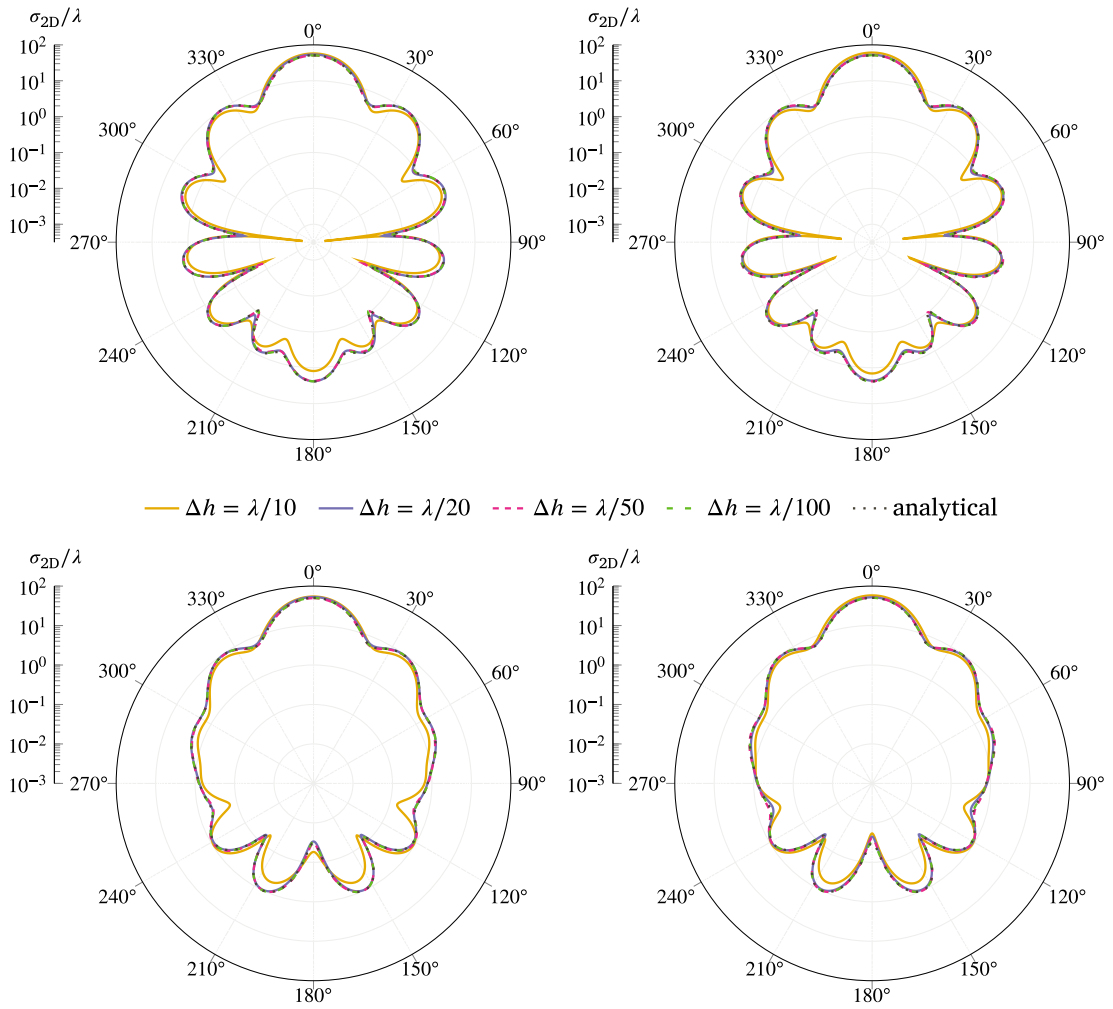


Fig. 11. Analytical and numerical RCS for TM (top row) and TE (bottom row) polarizations using *h*-FEM (left column) and IGFEM (right column).

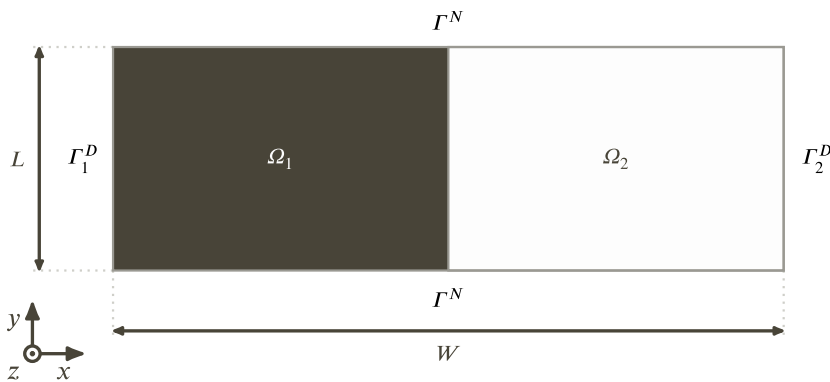


Fig. 12. Schematic of the problem with a single interface used to compare the convergence of IGFEM to the convergence of the method presented in Zou et al. [61].

A convergence analysis follows using only IGFEM for two frequencies $\omega = \{10/L, 20/L\}$ and for $h/L = \{1/50, 1/100, 1/200, 1/400\}$. The solution for $\omega = 20/L$ is shown in Fig. 13 with $h/L = 1/50$. The global measure of error in the L^2 -norm, which is computed using (36), is plotted against the mesh size in Fig. 14. Comparing to the convergence obtained by Zou et al. [61], it is shown that both methods obtain the same (optimal) convergence, with IGFEM yielding a slightly lower error.

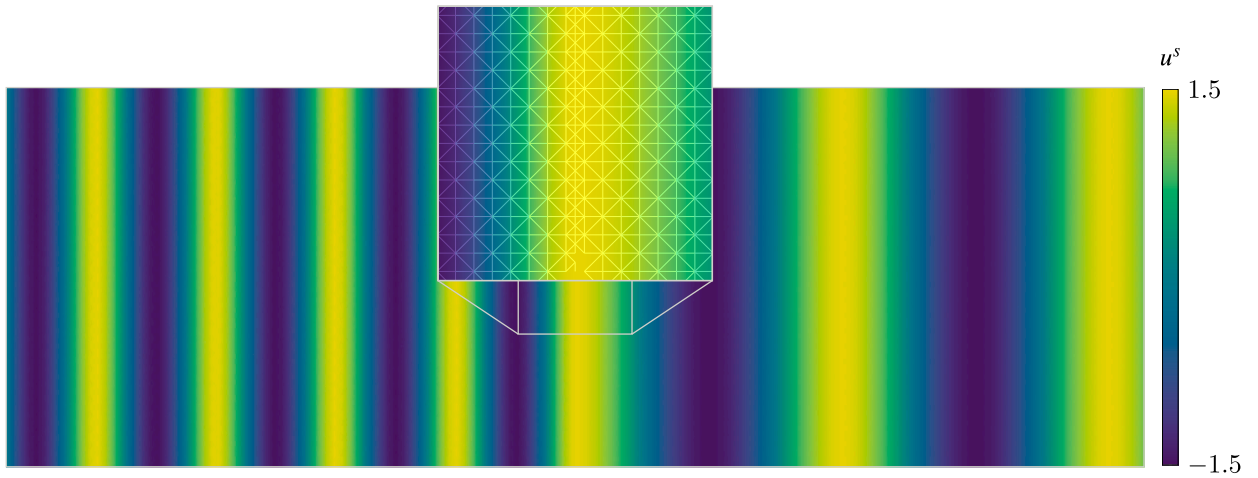


Fig. 13. The scattered field for $\omega = 20/L$, obtained via IGFEM.

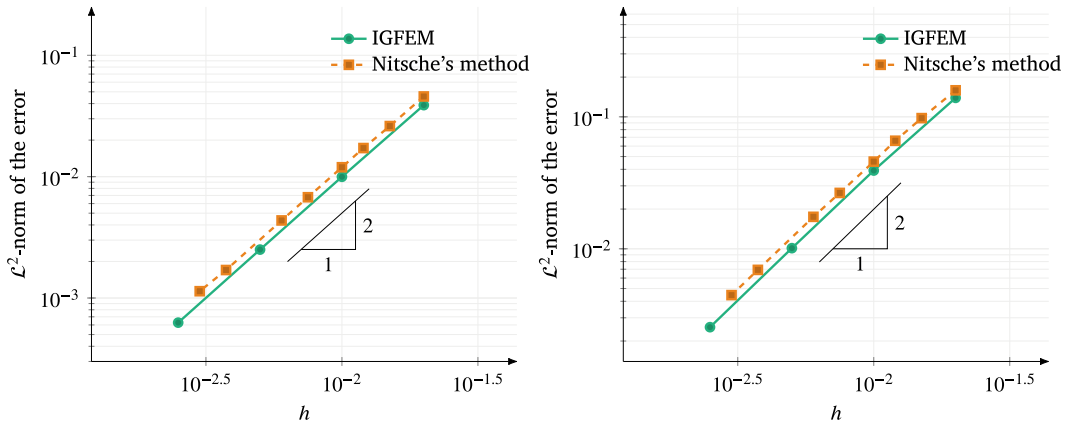


Fig. 14. L^2 -norm of the global error as a function of the mesh size h for $\omega^2 = 100$ (left) and $\omega^2 = 400$ (right).

3.4. Optimizing for energy concentration

The results of the previous section show that IGFEM can recover optimal convergence rates for the Mie scattering problem. We now combine IGFEM-based analysis with a level set description of topology, resulting in an interface-enriched level set-based procedure that can be used for topology optimization. Consider the optimization problem studied by Christiansen and Sigmund [65] (see Fig. 15), where we aim at maximizing the performances of both a 2D meta-lens and a reflector for an incident plane wave. The figure shows a schematic of both optimization problems, with $W = 2L$. The height of the dielectric substrate Ω_1 is $L_s = 0.1L$, the height of the design area Ω_d is $L_d = 0.075L$, and the thickness of the PML layer surrounding the domain Ω_3 is $t_{\text{PML}} = 0.175L$. The design area consists of both Ω_1 and Ω_2 , and the optimizer will determine the topology. x_f is the chosen focal point of the lens/reflector, Ω_2 is the surrounding vacuum ($\epsilon_{r,2} = 1$), and Γ^N is the boundary region with prescribed homogeneous Neumann boundary condition for symmetry. All domains have a relative permeability of $\mu_r = 1$. Two initial designs are used for both optimization problems, one consisting of dielectric material with circular vacuum domains and the other as the inverse, shown in Fig. 16; these will be referred to henceforth as the dielectric and vacuum initial designs, respectively. For all optimization problems all material interfaces will be resolved using IGFEM and a uniform mesh size of $h = \lambda/(10\epsilon_r)$ is used except for the design area Ω_d , where we use $h = \lambda/20$.

For the design of a metalens the electric field intensity is maximized at the focal point $x_f = (0, 0.6L)$ for an incident plane wave with wavelength $\lambda = 0.175L$ and an angle of incidence $\varphi = \pi/2$ (towards the positive y direction). The design material in this case has a relative permittivity $\epsilon_{r,1} = 2$. The optimization ran for 200 iterations. Fig. 17 shows the optimized metalens design and resulting electric field intensity. Very similar designs—and thus performance—were attained by starting the topology optimization with both initial designs. This can also be seen on the left in Fig. 19. However, the fact that the optimized designs are not exactly the same for the two initial design indicates the non-convexity of this topology optimization problem. For comparison purposes, the same optimization problem was solved using a density-based approach taken from Christiansen and Sigmund [65], using various

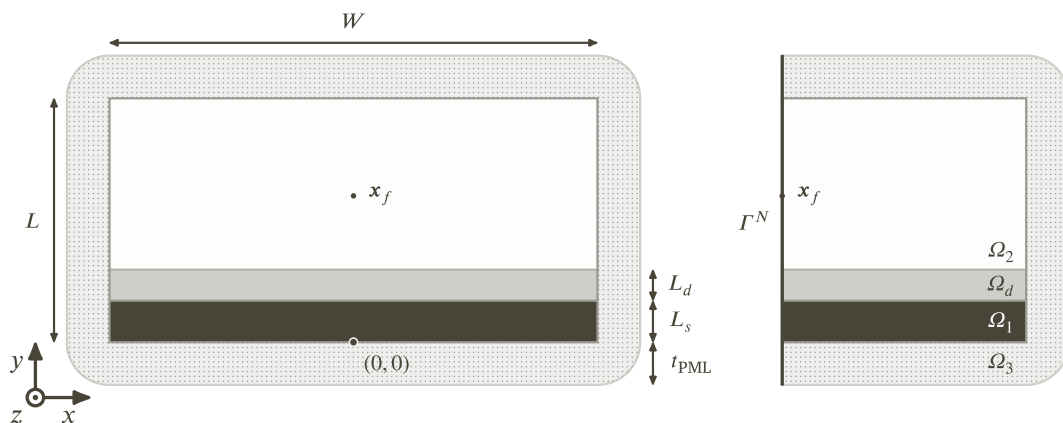


Fig. 15. Schematic of the optimization problem (left) and the computational domain used for the optimization accounting for symmetry (right).

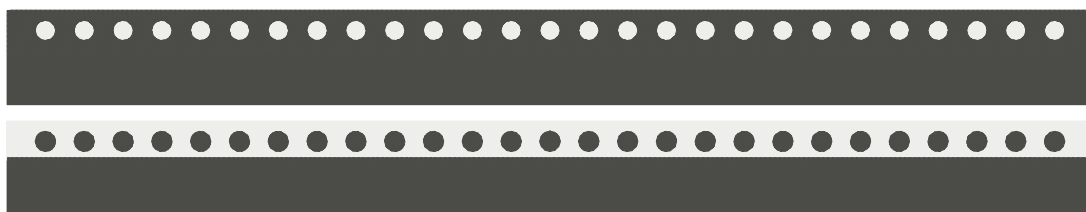


Fig. 16. Dielectric (top) and vacuum (bottom) initial designs used for the topology optimization of both the metalens and the reflector.

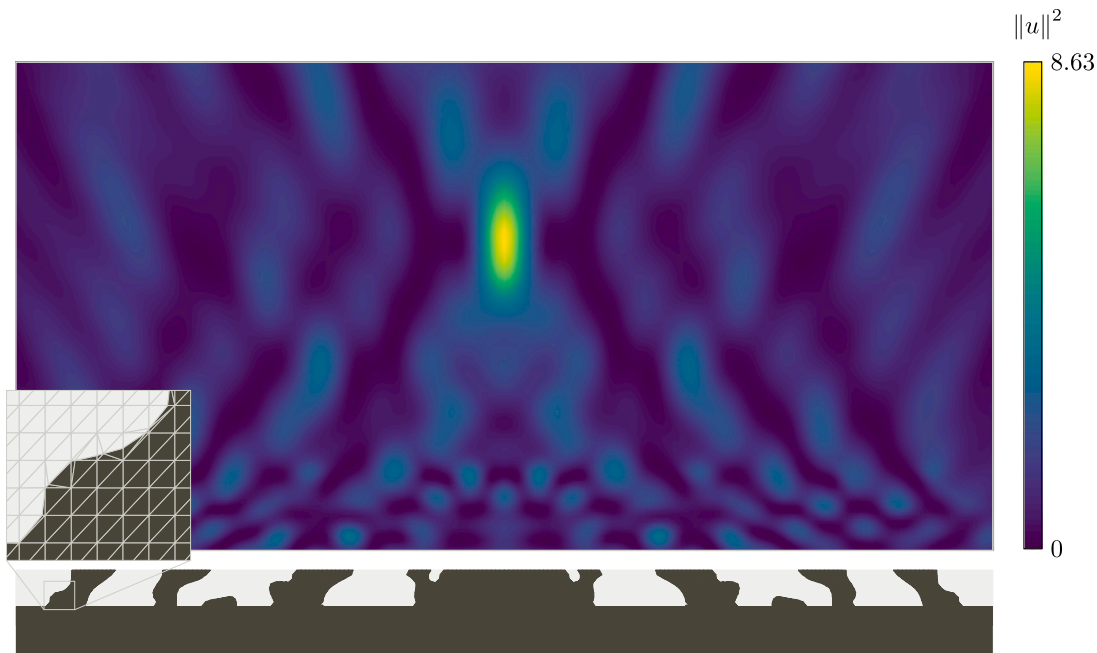


Fig. 17. The optimized metalens design (bottom) starting from the dielectric initial design together with the resulting electric field intensity (top).

filter radii. The density-based results are shown in Fig. 19 as grey lines. After the optimization process, the density-based designs are projected to black-and-white designs using a smoothed approximation of the Heaviside function, shown as grey markers in Fig. 19 [65]. It can be seen that the thresholding changes the performance of the designs, yielding mostly an improvement. The maximum light intensity obtained is ≈ 7.2 , whereas the maximum field strength using our method is ≈ 8.2 .

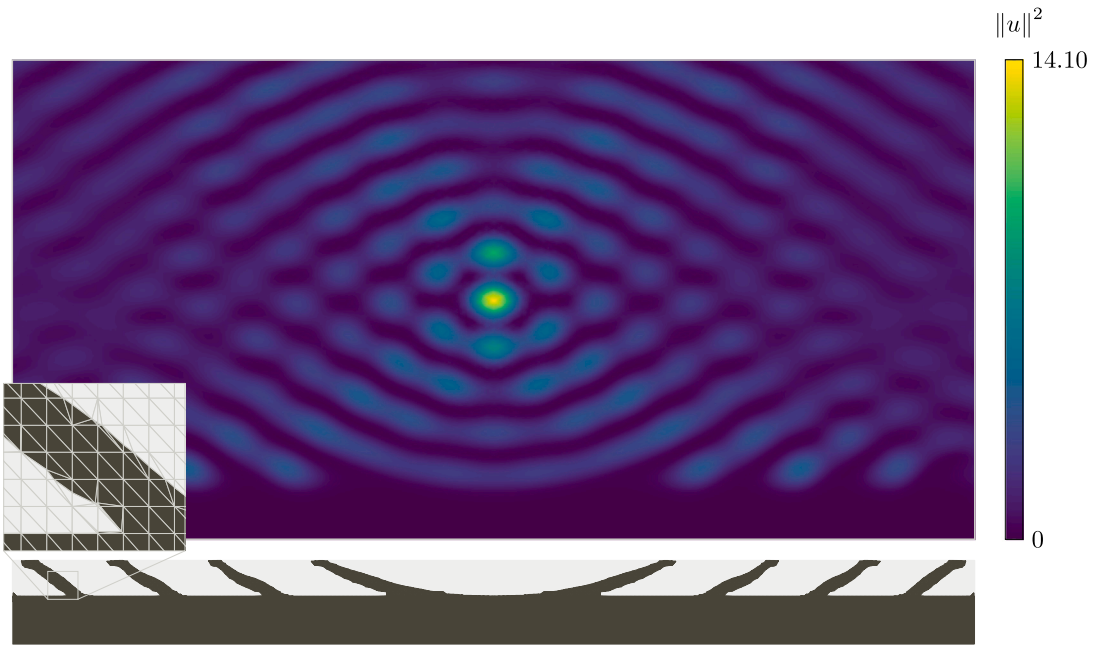


Fig. 18. The optimized reflector design (bottom) starting from the vacuum initial design together with the resulting electric field intensity (top).

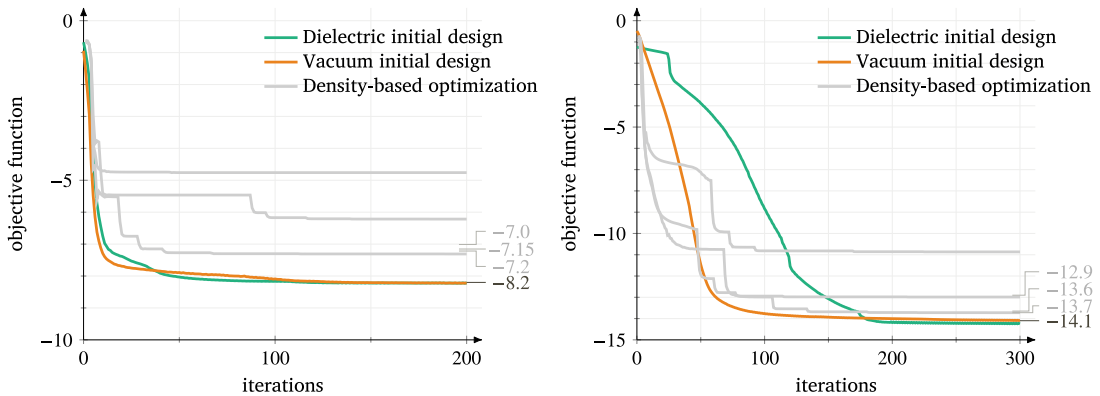


Fig. 19. The convergence of the metalens objective function (on the left) and the reflector objective function (on the right) for both initial designs. The density-based optimization results taken from Christiansen and Sigmund [65] for three different filter radii are shown in grey. The three grey markers show the performance of the density-based design after projecting to a black-and-white design.

For the design of a reflector the electric field intensity is maximized at the focal point $x_f = (0, 0.5L)$ for an incident plane wave with wavelength $\lambda = 0.175L$ and an angle of incidence $\varphi = -\pi/2$ (i.e., towards the negative y direction). The design material in this case has a relative permittivity $\epsilon_{r1} = 1.36 - 6.08j$. The optimization ran for 300 iterations. Fig. 18 shows the optimized reflector design and the resulting electric field intensity. The dielectric initial design resulted in a slightly better performance, but since the optimized design contained non-feasible geometry (in the form of disconnected material) the vacuum initial design is shown. Just like the metalens optimization, these results indicate we deal with a non-convex optimization problem. Again, the same optimization problem was solved using a density-based optimization using various filter radii. The maximum light intensity obtained is ≈ 13.7 , whereas the maximum field strength using our method is ≈ 14.1 .

4. Summary and conclusions

We introduced a 2-D interface-enriched generalized finite element method (IGFEM) for the computational analysis and design—by means of topology optimization—of nanophotonic devices. This method allows for the simulation of different geometries without the need for generating geometry-fitted meshes. Compared to similar methods, i.e., X/GFEM or SGFEM, IGFEM uses

enrichment functions that vanish at the original mesh nodes. This allows for a straightforward enforcement of essential boundary conditions and retains an accurate approximation in blending elements [62]. IGFEM's capabilities for band structure analysis were first demonstrated in the context of phononic crystals by van den Boom et al. [50]. Here we show that the band structure of photonic crystals can also be calculated accurately with IGFEM by comparing our results with standard FEM on the problem studied by Joannopoulos et al. [31]. A convergence analysis on a Mie scattering problem—for both TM and TE polarization cases—then showed that IGFEM recovered the optimal convergence rate expected for smooth problems. Moreover, a far-field analysis showed that the numerical RCS for both h -FEM and IGFEM (on fitted and unfitted meshes, respectively) approach the analytical solution as the mesh size is refined. Finally, a 2-D interface-enriched level set-based topology optimization procedure was presented, which can be used to design nanophotonic devices as an alternative procedure to density-based topology optimization methods commonly found in the literature. Two optimization problems were investigated, whereby the light intensity at a chosen point of both a 2-D meta lens and a 2-D reflector was maximized. Very small oscillations can be seen when the optimization is close to the optimum, which are possibly caused by the discretization of the level set function reducing the accuracy of the sensitivities, as discussed in van den Boom et al. [62]. Still, the results for both problems showed similarities with designs found in the literature. In fact, for both optimization problems, the results obtained using the proposed procedure are around 10% better than those obtained using the density-based optimization found in Christiansen and Sigmund [65]. However, the first-order ABC used in the density-based topology optimization is often not as accurate as the PML used in this paper [65,71]. Therefore, the different boundary conditions could partly be responsible for the differences in optimization results.

We compared our approach to Nitsche's method proposed by Zou et al. [61], and we showed that IGFEM retrieves the same convergence rate with a similar accuracy. However, we note that Nitsche's method mandates for a stabilization parameter that is obtained at element level to satisfy the inf-sup condition, and requires that the driving frequencies do not coincide with the eigenvalues of the stabilized coercive bilinear operator $a(\cdot, \cdot)$ [61]. Therefore, the enriched methodology herein does not only yield optimal convergence, but also has a simpler formulation and therefore a more straightforward implementation. Comparing our convergence rates to the enriched formulation that uses edge elements by Zhang et al. [60], we note that both methods achieve very similar error convergence as their standard finite element counterparts. A notable difference between using nodal and edge elements is that nodal elements converge twice as fast as edge (Whitney 1) elements in the L^2 -norm [59], and this of course extends naturally to their enriched counterparts. We also note that in the work of Zhang et al. [60] the error of the use of an first-order ABC becomes dominant at finer meshes, compared to the PML in this work which has higher accuracy. Once again we highlight that our approach is easier to implement than that of Zhang et al. [60] since it can use standard finite elements that do not satisfy the divergence-free property. It is worth noting, however, that the approach of Zhang et al. [60] extends naturally to 3-D. Extending our methodology to 3-D would require a means to prevent spurious solutions, for instance, by adding a penalty term to the formulation to enforce divergence conditions [57].

Finally, this work presents the first level set-based topology optimization procedure for electromagnetic problems using IGFEM-based analysis. The main advantage of IGFEM lies in its flexibility with regards to the choice of finite element discretizations, since these are completely decoupled from the topology of dielectric and vacuum phases. This decoupling is particularly interesting for topology optimization problems, where boundaries change throughout the optimization. From the optimization results we can conclude that further research is needed to investigate the relation between density-based optimization and the level set-based optimization using IGFEM-based analysis.

CRedit authorship contribution statement

Steven van Bergen: Writing – original draft, Software, Methodology, Investigation, Formal analysis, Conceptualization. **Richard A. Norte:** Writing – review & editing, Supervision, Methodology, Conceptualization. **Alejandro M. Aragón:** Writing – review & editing, Supervision, Methodology, Conceptualization.

Declaration of competing interest

The authors declare that they have no known competing financial interests or personal relationships that could have appeared to influence the work reported in this paper.

Data availability

No data was used for the research described in the article.

Appendix. Sensitivity analysis

The sensitivity to the optimization problem defined in Eq. (26) can be calculated with

$$\frac{\partial \Psi}{\partial d_i} = \frac{\partial \Psi}{\partial U_k} \frac{\partial U_k}{\partial \phi_j} \frac{\partial \phi_j}{\partial d_i}. \quad (37)$$

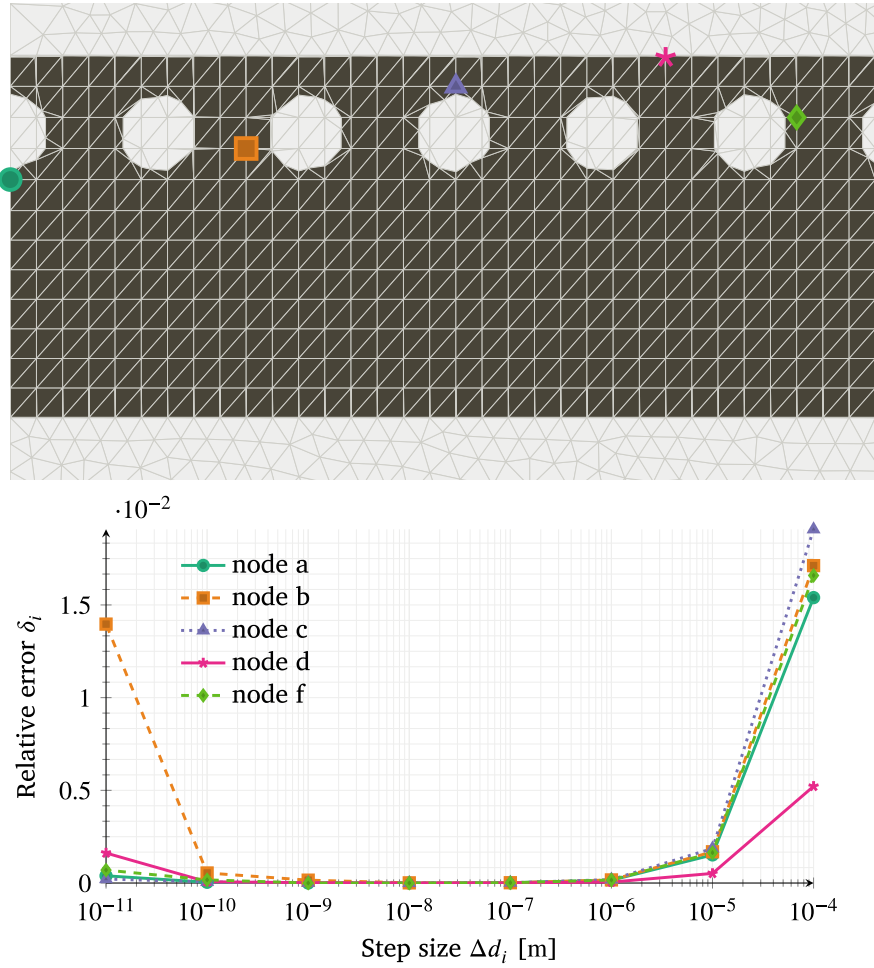


Fig. 20. The absolute relative error δ_i between sensitivities at 5 nodes calculated analytically or with a forward finite difference scheme for different step sizes Δd_i .

The first term is the derivative of the figure of merit with respect to the electric field values

$$\frac{\partial \Psi}{\partial U_k} = -2U_m^* P_{mk}, \quad (38)$$

where $*$ is the complex conjugate. The second term is the derivative of the electric field, with respect to every level set value, which can be calculated by first solving the linear equation

$$(\mathbf{K} - \omega^2 \mathbf{M}) \frac{\partial U_k^s}{\partial \phi_j} = \left(\frac{\partial \mathbf{K}}{\partial \phi_j} - \omega^2 \frac{\partial \mathbf{M}}{\partial \phi_j} \right) U_k^s - T \left[\left(\frac{\partial \mathbf{K}}{\partial \phi_j} - \omega^2 \frac{\partial \mathbf{M}}{\partial \phi_j} \right) \tilde{U}_k + (\mathbf{K} - \omega^2 \mathbf{M}) \frac{\partial \tilde{U}_k}{\partial \phi_j} \right], \quad (39)$$

to find the derivative of the scattered field, after which the derivative of the incoming field can be added to get the total field derivative with respect to every level set value. Here, \tilde{U} denotes the incoming field. The derivative of the system matrix with respect to a design variable can be calculated with

$$\frac{\partial \mathbf{K}}{\partial \phi_j} - \omega^2 \frac{\partial \mathbf{M}}{\partial \phi_j} = \sum_{l \in \iota_j} \sum_{e \in \iota_l} \left(\frac{\partial k_e}{\partial x_l} - \omega^2 \frac{\partial m_e}{\partial x_l} \right) \frac{\partial x_l}{\partial \phi_j}, \quad (40)$$

where ι_j is the set of enriched nodes which are influenced by the level set value ϕ_j , ι_l is the set of integration elements in the support of the enriched node x_l and

$$\frac{\partial x_l}{\partial \phi_j} = - \frac{\phi(x_k)}{(\phi(x_j) - \phi(x_k))^2} (x_j - x_k), \quad (41)$$

which is the design velocities of enriched node x_i , where x_j and x_l are the supporting nodes on the intersected edge from the original mesh. The term $\partial \bar{U}_k / \partial \phi_j$ only has nonzero values in i_j , which can be calculated by

$$\frac{\partial \bar{u}_i}{\partial \phi_j} = \sum_{l \in i_j} \left(\frac{\partial \bar{u}(x_l)}{\partial x_l} \frac{\partial x_l}{\partial \phi_j} - \sum_{j \in i_p} \frac{N_j(x_l)}{\partial x_l} \frac{\partial x_l}{\partial \phi_j} \bar{U}_j \right), \quad (42)$$

where the term $N_j(x_l) / \partial x_l$ is the change in shape function values at x_l when the enriched node moves and $\partial \bar{u}(x_l) / \partial x_l$ is the change in the incoming field value at x_l when the enriched node moves, which can be calculated by

$$\frac{\partial \bar{u}(x)}{\partial x} = -jk_0 \mu_0 e^{-jk_0(x \cos \varphi + y \sin \varphi)} \begin{bmatrix} \cos \varphi \\ \sin \varphi \end{bmatrix}. \quad (43)$$

Note that the enriched node scaling $1/(s_i \psi_i(x_i))$ that is present in Eq. (19) is set to 1 during optimization, hence why it is left out. Finally, the third term is the derivative of the nodal level set values with respect to the design variables, which is defined as

$$\frac{\partial \phi}{\partial d} = \theta^\top. \quad (44)$$

Then we also check our analytical sensitivities by computing the relative error with respect to finite difference sensitivities. The relative error is defined as

$$\delta_i = \frac{|\Psi'_i - \partial \Psi / \partial d_i|}{|\partial \Psi / \partial d_i|}, \quad (45)$$

where Ψ'_i is the sensitivity for node i calculated with the finite difference. This relative error was calculated for 5 non-zero design variables, the position of which are showed in Fig. 20, for different step sizes Δd_i . The resulting error shows the expected result where step sizes that are too large or small will result in a large error. For these 5 nodes, the optimal finite difference step size seems to be around $\Delta d_i = 1e - 8$ m.

References

- [1] A.F. Koenderink, A. Alù, A. Polman, Nanophotonics: Shrinking light-based technology, *Science* 348 (6234) (2015) 516–521, <http://dx.doi.org/10.1126/science.1261243>.
- [2] B. Jia, Nanophotonics silicon solar cells: status and future challenges, *Nanotechnol. Rev.* 4 (4) (2015) 337–346, <http://dx.doi.org/10.1515/ntrev-2015-0025>.
- [3] O. Painter, R.K. Lee, A. Scherer, A. Yariv, J.D. O'Brien, P.D. Dapkus, I. Kim, Two-dimensional photonic band-gap defect mode laser, *Science* 284 (5421) (1999) 1819–1821, <http://dx.doi.org/10.1126/science.284.5421.1819>.
- [4] W.R. Frei, H.T. Johnson, K.D. Choquette, Optimization of a single defect photonic crystal laser cavity, *J. Appl. Phys.* 103 (3) (2008) 1–7, <http://dx.doi.org/10.1063/1.2838173>.
- [5] A. Harhouz, A. Hocini, Design of high-sensitive biosensor based on cavity-waveguides coupling in 2D photonic crystal, *J. Electromagn. Waves Appl.* 29 (5) (2015) 659–667, <http://dx.doi.org/10.1080/09205071.2015.1012597>.
- [6] G. Pitruzzello, T.F. Krauss, Photonic crystal resonances for sensing and imaging, *J. Opt.* 20 (7) (2018) 1–23, <http://dx.doi.org/10.1088/2040-8986/aac75b>.
- [7] H. Altug, S.-H. Oh, S.A. Maier, J. Homola, Advances and applications of nanophotonic biosensors, *Nature Nanotechnol.* 17 (1) (2022) 5–16, <http://dx.doi.org/10.1038/s41565-021-01045-5>.
- [8] J.N. Anker, W.P. Hall, O. Lyandres, N.C. Shah, J. Zhao, R.P. Van Duyne, Biosensing with plasmonic nanosensors, *Nature Mater.* 7 (6) (2008) 442–453, <http://dx.doi.org/10.1038/nmat2162>.
- [9] G. Ruiz-Vega, M. Soler, L.M. Lechuga, Nanophotonic biosensors for point-of-care {COVID}-19 diagnostics and coronavirus surveillance, *J. Phys.: Photonics* 3 (1) (2021) 1100, <http://dx.doi.org/10.1088/2515-7647/abd4ee>.
- [10] S. Molesky, Z. Lin, A.Y. Piggott, W. Jin, J. Vučković, A.W. Rodriguez, Inverse design in nanophotonics, *Nat. Photonics* 12 (11) (2018) 659–670, <http://dx.doi.org/10.1038/s41566-018-0246-9>.
- [11] K. Ashida, M. Okano, M. Ohtsuka, M. Seki, N. Yokoyama, K. Koshino, M. Mori, T. Asano, S. Noda, Y. Takahashi, Ultrahigh-Q photonic crystal nanocavities fabricated by CMOS process technologies, *Opt. Express* 25 (15) (2017) 18165, <http://dx.doi.org/10.1364/OE.25.018165>.
- [12] T. Asano, B.-S. Song, Y. Akahane, S. Noda, Ultrahigh-Q nanocavities in two-dimensional photonic crystal slabs, *IEEE J. Sel. Top. Quantum Electron.* 12 (6) (2006) 1123–1134, <http://dx.doi.org/10.1109/JSTQE.2006.881639>.
- [13] M. Minkov, V. Savona, Automated optimization of photonic crystal slab cavities, *Sci. Rep.* 4 (2015) 5124, <http://dx.doi.org/10.1038/srep05124>.
- [14] Z. Zhang, M. Qiu, Small-volume waveguide-section high Q microcavities in 2D photonic crystal slabs, *Opt. Express* 12 (17) (2004) 3988, <http://dx.doi.org/10.1364/OPEX.12.003988>.
- [15] D. Wang, Z. Yu, Y. Liu, X. Guo, C. Shu, S. Zhou, J. Zhang, Ultrasmall modal volume and high Q factor optimization of a photonic crystal slab cavity, *J. Opt.* 15 (12) (2013) 125102, <http://dx.doi.org/10.1088/2040-8978/15/12/125102>.
- [16] F. Wang, B.S. Lazarov, O. Sigmund, On projection methods, convergence and robust formulations in topology optimization, *Struct. Multidiscip. Optim.* 43 (6) (2011) 767–784, <http://dx.doi.org/10.1007/s00158-010-0602-y>.
- [17] F. Meng, X. Huang, B. Jia, Bi-directional evolutionary optimization for photonic band gap structures, *J. Comput. Phys.* 302 (2015) 393–404, <http://dx.doi.org/10.1016/j.jcp.2015.09.010>.
- [18] J.K. Guest, J.H. Prévost, T. Belytschko, Achieving minimum length scale in topology optimization using nodal design variables and projection functions, *Internat. J. Numer. Methods Engrg.* 61 (2) (2004) 238–254, <http://dx.doi.org/10.1002/nme.1064>.
- [19] M. Zhou, B.S. Lazarov, F. Wang, O. Sigmund, Minimum length scale in topology optimization by geometric constraints, *Comput. Methods Appl. Mech. Engrg.* 293 (2015) 266–282, <http://dx.doi.org/10.1016/j.cma.2015.05.003>.
- [20] H. Men, K.Y.K. Lee, R.M. Freund, J. Peraire, S.G. Johnson, Robust topology optimization of three-dimensional photonic-crystal band-gap structures, *Opt. Express* 22 (19) (2014) 22632, <http://dx.doi.org/10.1364/OE.22.022632>.
- [21] R. Mattoso, L.H. Gabrielli, A.A. Novotny, Topology design optimization of nanophotonic devices for energy concentration, *Appl. Math. Model.* 104 (2022) 517–530, <http://dx.doi.org/10.1016/j.apm.2021.11.030>.
- [22] F. Wang, R.E. Christiansen, Y. Yu, J. Mørk, O. Sigmund, Maximizing the quality factor to mode volume ratio for ultra-small photonic crystal cavities, *Appl. Phys. Lett.* 113 (24) (2018) 241101, <http://dx.doi.org/10.1063/1.5064468>.

- [23] R.E. Christiansen, F. Wang, J. Mørk, O. Sigmund, Photonic cavity design by topology optimization, in: B. Panchapakesan, A. Attias (Eds.), *Proceedings of SPIE - Nanoengineering: Fabrication, Properties, Optics, Thin Films, and Devices XVI*, Vol. 11089, International Society for Optics and Photonics, SPIE, 2019, pp. 40–46, <http://dx.doi.org/10.1117/12.2529099>.
- [24] F. Wang, O. Sigmund, Optimization of photonic crystal cavities, in: 2017 International Conference on Numerical Simulation of Optoelectronic Devices (NUSOD), IEEE, 2017, pp. 39–40, <http://dx.doi.org/10.1109/NUSOD.2017.8009980>.
- [25] G. Isiklar, P.T. Kristensen, J. Mørk, O. Sigmund, R.E. Christiansen, On the trade-off between mode volume and quality factor in dielectric nanocavities optimized for Purcell enhancement, *Opt. Express* 30 (26) (2022) 47304, <http://dx.doi.org/10.1364/OE.474686>.
- [26] J.S. Jensen, O. Sigmund, Topology optimization of photonic crystal structures: a high-bandwidth low-loss T-junction waveguide, *J. Opt. Soc. Amer. B* 22 (6) (2005) 1191, <http://dx.doi.org/10.1364/JOSAB.22.001191>.
- [27] P.I. Borel, A. Harpoth, L.H. Frandsen, M. Kristensen, P. Shi, J.S. Jensen, O. Sigmund, Topology optimization and fabrication of photonic crystal structures, *Opt. Express* 12 (9) (2004) 1996, <http://dx.doi.org/10.1364/OPEX.12.001996>.
- [28] F. Wang, J.S. Jensen, O. Sigmund, Robust topology optimization of photonic crystal waveguides with tailored dispersion properties, *J. Opt. Soc. Amer. B* 28 (3) (2011) 387–397, <http://dx.doi.org/10.1364/JOSAB.28.000387>.
- [29] Y. Chen, F. Meng, G. Li, X. Huang, Topology optimization of photonic crystals with exotic properties resulting from Dirac-like cones, *Acta Mater.* 164 (2019) 377–389, <http://dx.doi.org/10.1016/j.actamat.2018.10.058>.
- [30] S.J. van den Boom, R. Abedi, F. van Keulen, A.M. Aragón, A level set-based interface-enriched topology optimization for the design of phononic crystals with smooth boundaries, *Comput. Methods Appl. Mech. Engrg.* 408 (2023) 115888, <http://dx.doi.org/10.1016/j.cma.2023.115888>.
- [31] J.D. Joannopoulos, S.G. Johnson, J.N. Winn, R.D. Meade, *Photonic Crystals: Molding the Flow of Light*, second ed., Princeton University Press, Princeton and Oxford, 2008.
- [32] H. Hagino, Y. Takahashi, Y. Tanaka, T. Asano, S. Noda, Effects of fluctuation in air hole radii and positions on optical characteristics in photonic crystal heterostructure nanocavities, *Phys. Rev. B* 79 (8) (2009) 085112, <http://dx.doi.org/10.1103/PhysRevB.79.085112>.
- [33] T. Asano, B.-S. Song, S. Noda, Analysis of the experimental q factors (< 1 million) of photonic crystal nanocavities, *Opt. Express* 14 (5) (2006) 1996–2002, <http://dx.doi.org/10.1364/OE.14.001996>.
- [34] W.R. Frei, H.T. Johnson, Finite-element analysis of disorder effects in photonic crystals, *Phys. Rev. B* 70 (16) (2004) 165116, <http://dx.doi.org/10.1103/PhysRevB.70.165116>.
- [35] G. Allaire, F. Jouve, A.-M. Toader, Structural optimization using sensitivity analysis and a level-set method, *J. Comput. Phys.* 194 (1) (2004) 363–393, <http://dx.doi.org/10.1016/j.jcp.2003.09.032>.
- [36] J.S. Jensen, O. Sigmund, Topology optimization for nano-photonics, *Laser Photonics Rev.* 5 (2) (2011) 308–321, <http://dx.doi.org/10.1002/lpor.201000014>.
- [37] S.R. Idelsohn, J.M. Gimenez, J. Marti, N.M. Nigro, Elemental enriched spaces for the treatment of weak and strong discontinuous fields, *Comput. Methods Appl. Mech. Engrg.* 313 (2017) 535–559, <http://dx.doi.org/10.1016/j.cma.2016.09.048>.
- [38] C. Narvaez, M.R. Hashemi, P.B. Ryzhakov, J. Pons-Prats, H. Owen, Enriched finite element approach for modeling discontinuous electric field in multi-material problems, *Finite Elem. Anal. Des.* 225 (2023) 104007, <http://dx.doi.org/10.1016/j.finel.2023.104007>.
- [39] C. Narvaez, M.R. Hashemi, P.B. Ryzhakov, J. Pons-Prats, An enriched finite element/level-set model for two-phase electrohydrodynamic simulations, *Phys. Fluids* 35 (1) (2023) 012004, <http://dx.doi.org/10.1063/5.0127274>.
- [40] N. Moës, J. Dolbow, T. Belytschko, A finite element method for crack growth without remeshing, *Internat. J. Numer. Methods Engrg.* 46 (1) (1999) 131–150, [http://dx.doi.org/10.1002/\(SICI\)1097-0207\(19990910\)46:1<131::AID-NME726>3.0.CO;2-J](http://dx.doi.org/10.1002/(SICI)1097-0207(19990910)46:1<131::AID-NME726>3.0.CO;2-J).
- [41] C.A. Duarte, I. Babuška, J.T. Oden, Generalized finite element methods for three-dimensional structural mechanics problems, *Comput. Struct.* 77 (2) (2000) 215–232, [http://dx.doi.org/10.1016/S0045-7949\(99\)00211-4](http://dx.doi.org/10.1016/S0045-7949(99)00211-4).
- [42] N. Duan, W. Xu, S. Wang, H. Li, Y. Guo, J. Zhu, Extended finite element method for electromagnetic fields, in: 2015 IEEE International Conference on Applied Superconductivity and Electromagnetic Devices (ASEMD), IEEE, 2015, pp. 364–365, <http://dx.doi.org/10.1109/ASEMD.2015.7453614>.
- [43] C. Siefert, T.E. Voth, P.B. Bochev, Electromagnetic eXtended finite elements for accurate resolution of multi-material cells, in: *The ARL 2012 Research in Ballistic Protection Technologies Workshop*, 2012.
- [44] N. Duan, W. Xu, S. Wang, J. Zhu, Y. Guo, An improved XFEM with multiple high-order enrichment functions and low-order meshing elements for field analysis of electromagnetic devices with multiple nearby geometrical interfaces, *IEEE Trans. Magn.* 51 (3) (2015) 1–4, <http://dx.doi.org/10.1109/TMAG.2014.2358792>.
- [45] N. Duan, W. Xu, S. Wang, J. Zhu, Accuracy analysis of structure with nearby interfaces within XFEM, *AIP Adv.* 7 (5) (2017) 056011, <http://dx.doi.org/10.1063/1.4974983>.
- [46] R. Adriano, W.G. Facco, E.J. Silva, A modified plane wave enrichment to solve 2-D electromagnetic problems using the generalized finite-element method, *IEEE Trans. Magn.* 51 (3) (2015) 1–4, <http://dx.doi.org/10.1109/TMAG.2014.2362102>.
- [47] S. Jeong, S. Lim, S. Min, Level-set-based topology optimization using remeshing techniques for magnetic actuator design, *IEEE Trans. Magn.* 52 (3) (2016) 1–4, <http://dx.doi.org/10.1109/TMAG.2015.2485260>.
- [48] I. Babuška, U. Banerjee, Stable generalized finite element method (SGFEM), *Comput. Methods Appl. Mech. Engrg.* 201–204 (2012) 91–111, <http://dx.doi.org/10.1016/j.cma.2011.09.012>.
- [49] S.J. van den Boom, J. Zhang, F. Keulen, A.M. Aragón, A stable interface-enriched formulation for immersed domains with strong enforcement of essential boundary conditions, *Internat. J. Numer. Methods Engrg.* 120 (2019) 1163–1183, <http://dx.doi.org/10.1002/nme.6139>.
- [50] S.J. van den Boom, F. van Keulen, A.M. Aragón, Fully decoupling geometry from discretization in the Bloch–Floquet finite element analysis of phononic crystals, *Comput. Methods Appl. Mech. Engrg.* 382 (2021) 113848, <http://dx.doi.org/10.1016/j.cma.2021.113848>.
- [51] S. Soghrati, A.M. Aragón, C.A. Duarte, P.H. Geubelle, An interface-enriched generalized FEM for problems with discontinuous gradient fields, *Internat. J. Numer. Methods Engrg.* 89 (8) (2012) 991–1008, <http://dx.doi.org/10.1002/nme.3273>.
- [52] A.M. Aragón, B. Liang, H. Ahmadian, S. Soghrati, On the stability and interpolating properties of the Hierarchical Interface-enriched Finite Element Method, *Comput. Methods Appl. Mech. Engrg.* 362 (2020) 112671, <http://dx.doi.org/10.1016/j.cma.2019.112671>.
- [53] J. Haslinger, Y. Renard, A new fictitious domain approach inspired by the extended finite element method, *SIAM J. Numer. Anal.* 47 (2) (2009) 1474–1499, <http://dx.doi.org/10.1137/070704435>.
- [54] K. Zhang, J.-M. Jin, P.H. Geubelle, A 3-D interface-enriched generalized FEM for electromagnetic problems with nonconformal discretizations, *IEEE Trans. Antennas and Propagation* 63 (12) (2015) 5637–5649, <http://dx.doi.org/10.1109/TAP.2015.2489217>.
- [55] K. Zhang, A.R. Najafi, P.H. Geubelle, J.-M. Jin, A 2D interface-enriched generalized FEM for EM analysis of composite materials, in: 2015 IEEE International Symposium on Antennas and Propagation & USNC/URSI National Radio Science Meeting, IEEE, 2015, pp. 171–172, <http://dx.doi.org/10.1109/APS.2015.7304471>.
- [56] K. Zhang, A.R. Najafi, P.H. Geubelle, J.-M. Jin, Gradient-based shape optimization for electromagnetic problems using IGFEM, in: 2016 IEEE International Symposium on Antennas and Propagation (APSURSI), IEEE, 2016, pp. 579–580, <http://dx.doi.org/10.1109/APS.2016.7695998>.
- [57] J.-M. Jin, *The Finite Element Method in Electromagnetics*, second ed., John Wiley & Sons, Ltd., 2002.
- [58] J.C. Nedelec, Mixed finite elements in \mathbb{R}^3 , *Numer. Math.* 35 (3) (1980) 315–341, <http://dx.doi.org/10.1007/BF01396415>.
- [59] G. Mur, Edge elements, their advantages and their disadvantages, *IEEE Trans. Magn.* 30 (5) (1994) 1460–1465, <http://dx.doi.org/10.1109/20.312706>.

- [60] K. Zhang, A.R. Najafi, J.-M. Jin, P.H. Geubelle, An interface-enriched generalized finite element analysis for electromagnetic problems with non-conformal discretizations, *Int. J. Numer. Modelling, Electron. Netw. Devices Fields* 29 (2) (2016) 265–279, <http://dx.doi.org/10.1002/jnm.2073>.
- [61] Z. Zou, W. Aquino, I. Harari, Nitsche's method for Helmholtz problems with embedded interfaces, *Internat. J. Numer. Methods Engrg.* 110 (7) (2017) 618–636, <http://dx.doi.org/10.1002/nme.5369>.
- [62] S.J. van den Boom, J. Zhang, F. van Keulen, A.M. Aragón, An interface-enriched generalized finite element method for level set-based topology optimization, *Struct. Multidiscip. Optim.* 63 (1) (2021) 1–20, <http://dx.doi.org/10.1007/s00158-020-02682-5>.
- [63] J. Zhang, F. van Keulen, A.M. Aragón, On tailoring fracture resistance of brittle structures: A level set interface-enriched topology optimization approach, *Comput. Methods Appl. Mech. Engrg.* 388 (2022) 114189, <http://dx.doi.org/10.1016/j.cma.2021.114189>.
- [64] A. Souto, J. Zhang, A.M. Aragón, K.P. Velikov, C. Coulais, Edible mechanical metamaterials with designed fracture for mouthfeel control, *Soft Matter* 18 (15) (2022) 2910–2919, <http://dx.doi.org/10.1039/D1SM01761F>.
- [65] R.E. Christiansen, O. Sigmund, Compact 200 line MATLAB code for inverse design in photonics by topology optimization: tutorial, *J. Opt. Soc. Amer. B* 38 (2) (2021) 510–520, <http://dx.doi.org/10.1364/JOSAB.405955>.
- [66] A.M. Aragón, C.A. Duarte, *Fundamentals of Enriched Finite Element Methods*, first ed., Elsevier, 2023.
- [67] S. Koziel, X. Yang, Q. Zhang, *Simulation-Driven Design Optimization and Modeling for Microwave Engineering*, first ed., Imperial College Press, 2013, <http://dx.doi.org/10.1142/p860>.
- [68] A.C. Polycarpou, *Introduction to the Finite Element Method in Electromagnetics*, first ed., Morgan & Claypool, 2006.
- [69] Ö. Özgün, M. Kuzuoğlu, *MATLAB®-Based Finite Element Programming in Electromagnetic Modeling*, first ed., CRC Press, 2018, <http://dx.doi.org/10.1201/9780429457395>.
- [70] J.-M. Jin, *Theory and Computation of Electromagnetic Fields*, second ed., John Wiley & Sons, Ltd., 2015.
- [71] J.-M. Jin, D.J. Riley, *Finite Element Analysis of Antennas and Arrays*, first ed., John Wiley & Sons, Ltd., 2009.
- [72] K. Svanberg, The method of moving asymptotes—a new method for structural optimization, *Internat. J. Numer. Methods Engrg.* 24 (2) (1987) 359–373, <http://dx.doi.org/10.1002/nme.1620240207>.
- [73] C.A. Balanis, *Advanced Engineering Electromagnetics*, second ed., John Wiley & Sons, Ltd., 2012.